

The East Greenland Caledonides—teleseismic signature, gravity and isostasy

Christian Schiffer,¹ Bo Holm Jacobsen,¹ Niels Balling,¹ Jörg Ebbing²
and Søren Bom Nielsen¹

¹Department of Geoscience, Aarhus University, Høegh-Guldbergs gade 2, DK-8000, Aarhus C, Denmark. E-mail: christian.schiffer@geo.au.dk

²Institute of Geosciences, Department of Geophysics, Kiel University, Otto-Hahn-Platz 1, D-24118, Kiel, Germany

Accepted 2015 September 3. Received 2015 August 20; in original form 2015 June 23

SUMMARY

The large-scale geological evolution of the North Atlantic Realm during the past 450 Myr is largely understood, but crucial elements remain uncertain. These involve the Caledonian orogeny, the formation of the North Atlantic and accompanying igneous activity, and the present-day high topography surrounding the North Atlantic. Teleseismic receiver function interpretation in the Central Fjord Region of East Greenland recently suggested the presence of a fossil Caledonian subduction complex, including a slab of eclogitised mafic crust and an overlying wedge of serpentinised mantle peridotite. Here we further investigate this topic using inverse receiver functions modelling. The obtained velocity models are tested with regard to their consistency with the regional gravity field and topography. We find that the obtained receiver function model is generally consistent with gravity and isostasy. The western part of the section, with topography of >1000 m, is clearly supported by the 40-km-thick crust. The eastern part requires additional buoyancy as provided by the hydrated mantle wedge. The geometry, velocities and densities are consistent with interpretation of the lithospheric structure as a fossil subduction zone complex. The spatial relations with Caledonian structures suggest a Caledonian origin. The results indicate that topography is isostatically compensated by density variations within the lithosphere, and that significant dynamic topography is not required at the present-day.

Key words: Body waves; Subduction zone processes; Dynamics of lithosphere and mantle; Crustal structure; Atlantic Ocean.

1 INTRODUCTION

The geology of the North Atlantic Realm (NAR) has been studied for more than a century so that the large-scale geological evolution in this region during the past 450 Myr is quite well understood. This makes the region an ideal testing ground for a number of geoscience problems, including the formation of the Caledonian mountain ranges (at approximately 425 Ma), the break-up of the North Atlantic and accompanying igneous activity (approximately 60 Ma), and the present-day high topography surrounding the North Atlantic.

The Caledonian orogenic evolution is commonly assessed by studies of the surface geology and structural trends, the deeper crustal structure, and dating of metamorphism and orogenic intrusions. While the surface geology in Scandinavia is well-studied, important Caledonian structures in East Greenland, such as the Caledonian Deformation Front and the Caledonian foreland basin, are likely to be covered by the ice sheet (Henriksen & Higgins 2008). The available Caledonian structural expression indicates a

generally bivertent orogen (Roberts 2003; Gee *et al.* 2008; Leslie *et al.* 2008). Caledonian metamorphic rocks and intrusions show ages from 500 to 360 Ma in the East Greenland and Scandinavian Caledonides (Gasser 2013; Corfu *et al.* 2014) indicating a complex and prolonged Caledonian evolution with multiple collision and subduction events. The exposed Caledonian structures are strongly modified by post-Caledonian extensional tectonism with reactivation of older thrusts (Fossen 2010) and significant erosion (Nielsen *et al.* 2009a; Medvedev *et al.* 2013; Medvedev & Hartz 2015).

Deep geophysical studies have been carried out along the East Greenland and Norwegian margins, although the data coverage clearly favours the Norwegian margin. Geophysical data provide estimates of crustal structure and Moho depth and, together with thermochronology, form the basis for assessing orogenic crustal thickening, extensional evolution and isostatic compensation. The extensive study of the crustal and lithospheric structure of the Scandinavian Caledonides has led to the consensus that its topography is isostatically compensated, mainly through thickened crust and variations in lithospheric thickness and composition (Ebbing *et al.*

2012; Gradmann *et al.* 2013; Maupin *et al.* 2013). The small amount of available data from East Greenland also indicate thickened crust beneath the Caledonian high topography (Schmidt-Aursch & Jokat 2005; Braun *et al.* 2007; Voss *et al.* 2009). Regional seismological studies provide information on the lithosphere and upper mantle (Darbyshire *et al.* 2004; Rickers *et al.* 2013).

Recent receiver function imaging of teleseismic waveforms at 11 broadband stations in the Central Fjord Region (CF) of East Greenland revealed an east-dipping structure interpreted as a fossil subduction zone of early Caledonian age, comprising a stagnated slab of eclogitised mafic crust overlain by a partly serpentinised mantle wedge (Schiffer *et al.* 2014).

Dipping linear structures in the upper mantle are observed worldwide and are frequently associated with subduction, collision and suturing events. Such structures are frequently imaged by near-vertical seismic reflection or wide-angle seismic refraction profiling (Balling 2000; van der Velden & Cook 2005; Clowes *et al.* 2010; Queity & Clowes 2010), but also by teleseismic receiver function analysis (Bostock 1998; Kind *et al.* 2002; Mercier *et al.* 2008; Rondenay *et al.* 2008; Bostock 2013).

In this study, we further investigate this model by inverse receiver function modelling of the above-mentioned broadband data. The direct gravitational and isostatic response of the derived geometry and associated density structure will be tested. This will provide important additional constraints regarding the composition, nature and origin of the deep subsurface of the East Greenland Caledonides.

2 GEOLOGICAL BACKGROUND

The dominant geological and topographic feature in the CF region is the remnants of the Caledonian Orogen. This mountain range formed after the collision of three palaeocontinents, Laurentia, Baltica and Avalonia, as well as several microcontinents and terranes during the closure of the Iapetus Ocean in the late Palaeozoic (Gee *et al.* 2008; Cocks & Torsvik 2011) as part of the Caledonian–Appalachian fold belt.

After a long period of passive lithospheric relaxation and post-orogenic collapse (Andersen *et al.* 1991; Fossen 2010), active intracratonic rifting initiated and transitioned into continental break-up. The formation of North Atlantic oceanic crust and lithosphere was accompanied by extensive igneous activity forming the North Atlantic Igneous Province (NAIP; Larsen & Saunders 1998; Tegner *et al.* 1998; Skogseid *et al.* 2000). This igneous event is commonly associated with a mantle plume (Fitton *et al.* 1997; Saunders *et al.* 1997; Brown & Lesher 2014) but also non-plume models are proposed (Korenaga & Kelemen 2000; Korenaga 2004; Foulger *et al.* 2005; Foulger & Anderson 2005).

Today, the North Atlantic is surrounded by areas of high-elevation and low-relief topography. The occurrence of this distinct topographic expression has been a matter of debate. One explanation is that these landscapes are peneplains created by erosion of ancient topography to sea level and more recently uplifted to their present elevation (Japsen & Chalmers 2000; Lidmar-Bergström & Näslund 2002; Green *et al.* 2013). This model might indicate a still present dynamic support (Rickers *et al.* 2013). Contrary to this, others favour models where the present topography constitutes remnants of the original Palaeozoic Caledonian mountain ranges preserved due to slow, climatically controlled erosion (Egholm *et al.* 2009; Nielsen *et al.* 2009b; Pedersen *et al.* 2010).

While the general tectonic elements of the Caledonian orogeny are understood (Roberts 2003; Gee *et al.* 2008; Leslie *et al.* 2008;

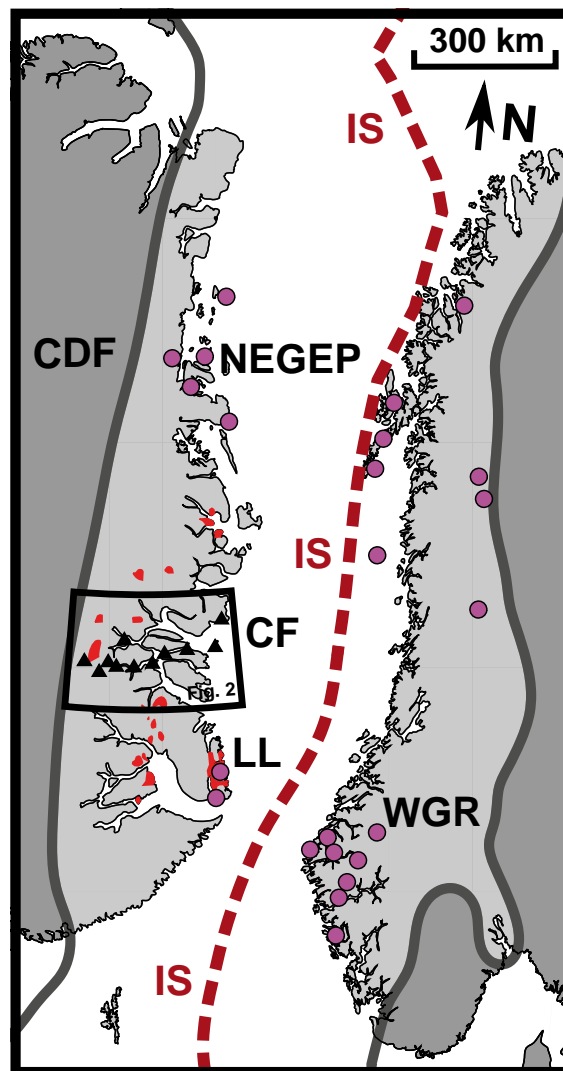


Figure 1. Palaeogeography of the Scandinavian and East Greenland Caledonides after collision of Laurentia and Baltica at about 425 Ma (after Cocks & Torsvik 2005, 2011). Grey line: Caledonian deformation front (CDF; Gee *et al.* 2008). Red line – Iapetus suture (IS; Cocks & Torsvik 2005). Black triangles – stations of the CF array. Pink circles – major occurrences of Caledonian eclogites (Fossen 2010). Red – Caledonian granites (Henriksen 1999). NEGEP – North East Greenland Eclogite Province, LL – Liverpool Land eclogite terrane, WGR – Western Gneiss Region. Black mark-up shows the area illustrated in Fig. 2.

Cocks & Torsvik 2011), the details of timing, direction, location and the number of involved subduction events are poorly resolved. The collisional history is usually constrained by the structural record, the basement affinity and the age of Caledonian metamorphism and orogenic intrusions. This is supported by the deep structural record made available by geophysical studies. The tectonic expression of the collisional history of this Himalayan-type orogeny (Gee *et al.* 2008) is preserved both in Scandinavia and in East Greenland where it is, however, limited by the overlying ice sheet (Henriksen 1999).

The main Scandian phase at approximately 425 Ma (continent–continent collision between Baltica and Laurentia, Fig. 1) is mainly supported by dating of high pressure rocks in the Western Gneiss Region of Norway (Dobrzynetskiya *et al.* 1995; van Roermund & Drury 1998; Hacker & Gans 2005) and Liverpool Land in East Greenland (Augland *et al.* 2010; Johnston *et al.* 2010), as well as

Central Fjord Region

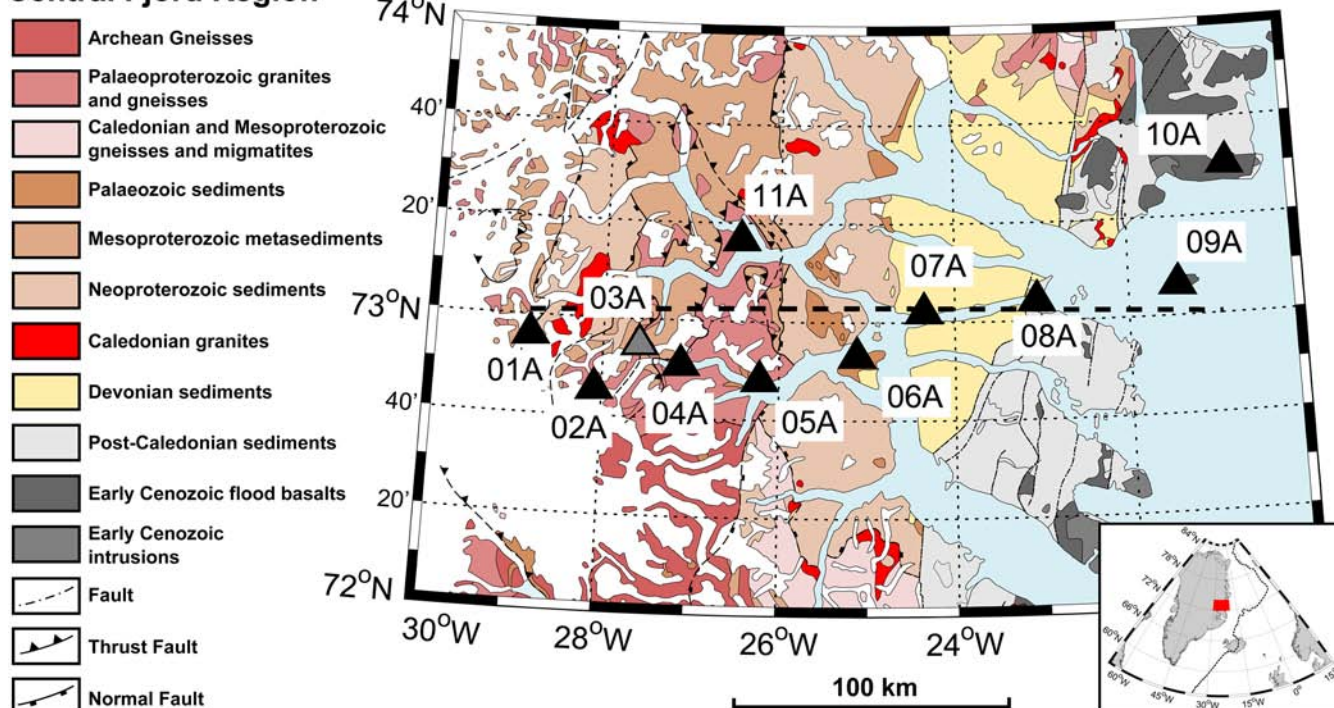


Figure 2. Geological map of the Central Fjord Region (after Henriksen 1999). Black triangles – station positions of the CF array, with station identification numbers. Grey triangle – station 03A, not included in this study; black stippled line – vertical projection plane of the receiver function model. Inset shows an overview of the North Atlantic and the location of the map.

orogenic S-type granitic intrusions in East Greenland (Kalsbeek *et al.* 2008).

Generally younger metamorphic ages of down to ~ 360 Ma have been identified in the Northeast Greenland Eclogite Province (NEGEP) and indicate a late compressional event in the Caledonides (Gilotti & McClelland 2007; Gilotti *et al.* 2014). Older ages (435–500 Ma) of igneous and metamorphic rocks in the Scandinavian Caledonides (Steltenpohl *et al.* 2003; Corfu *et al.* 2014) indicate an early Caledonian orogenic phase and accretion of magmatic arcs. This is corroborated by I-type granitic intrusions of similar ages (455–422 Ma) in the East Greenland Caledonides (Kalsbeek *et al.* 2008).

This evidence has led to departures from a simple model of only west-dipping Scandian subduction and collision. Other models include scenarios with an additional early west-dipping (Brueckner & van Roermund 2004; Brueckner 2006) or east-dipping subduction event (Yoshinobu *et al.* 2002; Andréasson *et al.* 2003; Roberts 2003; Gee *et al.* 2008). Late intracratonic eastward underthrusting (Gilotti & McClelland 2011) has also been suggested. Early Caledonian east-dipping subduction is in accordance with similar events identified in the northern Appalachians (Taconian phase; Karabinos *et al.* 1998; van Staal *et al.* 2009) and British Caledonides (Grampian phase; Van Staal *et al.* 1998; Dewey 2005).

The exposed surface geology of the East Greenland Caledonides is briefly summarised here (Gee 2005; Higgins & Leslie 2008; Gasser 2013; also consult Fig. 2). The Caledonian Fold Belt in East Greenland is divided into three major thrust sheets lying on top of Laurentian basement. These consist of mainly Archean-to-Palaeoproterozoic gneisses, alternating with Mesoproterozoic metasediments and Neoproterozoic sediments as well as migmatites, and approximately comprise the western half of the exposed rocks in central East Greenland. Granitic intrusions and Caledonian fore-

land windows are locally abundant. The eastern half is dominated by post-Caledonian sedimentary basins that formed since the Devonian. Close to the coastline these sediments locally alternate with Tertiary flood basalts and intrusions.

Geophysical evidence from the Scandinavian Caledonides along the Norwegian margin established the crustal and upper mantle structure and showed that there is a considerable thickness of crust beneath a large part of the region, indicating remnants of the Caledonian orogeny (Kinck *et al.* 1993; Iwasaki *et al.* 1994; Ottemöller & Midzi 2003; Svenningsen *et al.* 2007; Köhler *et al.* 2011; Stratford & Thybo 2011; England & Ebbing 2012; Kolstrup *et al.* 2012; Frassetto & Thybo 2013; Kolstrup & Maupin 2013). This thick crust provides a large part of the isostatic compensation of the Scandinavian Caledonides, together with variations in lithospheric thickness and composition (Ebbing *et al.* 2012; Gradmann *et al.* 2013; Maupin *et al.* 2013). The high topography of the Scandinavian Mountains generally correlates well with negative Bouguer anomalies (Balling 1980; Ebbing 2007).

Much sparser evidence from wide-angle seismic studies in East Greenland, some reaching deep into the fjords, indicates crust of 40–48 km in thickness beneath the high Caledonian topography along the East Greenland margin from 70°N to 74°N (Weigel *et al.* 1995; Mandler & Jokat 1998; Schlindwein & Jokat 1999; Schmidt-Aursch & Jokat 2005; Voss *et al.* 2009). This is corroborated by region-wide gravity modelling (Schmidt-Aursch & Jokat 2005; Braun *et al.* 2007). The crustal thickness shows an abrupt decrease to a relatively constant transitional segment of 25–30 km terminated by the continent–ocean transition approximately 250 km east of the coastline. Further data to the south and north are limited to offshore areas focusing on the magmatic passive continental margin (Fechner & Jokat 1996; Korenaga *et al.* 2000; Holbrook *et al.* 2001; Hopper *et al.* 2003; Voss & Jokat 2007). Receiver function studies of the

few permanent stations in East Greenland commonly show rather shallow Moho depths of 23–35 km near the coast (Dahl-Jensen *et al.* 2003; Kumar *et al.* 2007). Surface wave studies have also been conducted, using the available permanent and temporary stations in Greenland and the surrounding areas, and they provide indications for the thickness of the lithosphere (Darbyshire *et al.* 2004). The continental areas are otherwise poorly studied.

Recently, deep receiver function imaging from 11 broad-band seismometers located in the CF region of East Greenland at 73°N revealed an east-dipping structure in the upper mantle (Schiffer *et al.* 2014). This structure first appears at the base of the crust at approximately 40 km depth at the western end of the array in the centre of the Caledonian high topography, and reaches a depth of 100 km or more at the eastern limit, close to the coastline. The teleseismic signature along the CF array (Schiffer *et al.* 2014) suggests a downward velocity increase, indicated by ‘positive’ signals (by convention red), followed by a slightly weaker ‘negative’ signal (by convention blue), which suggests a downward velocity decrease. Together, these two conversions form a well-confined 10–15 km thin high velocity zone. Forward ‘2.5-D’ numerical RF modelling showed that P -wave velocities of 8.4 km s^{-1} in the background of ambient mantle velocities of 8.05 km s^{-1} convincingly reproduce the observed image. The seismological signature, forward modelling, the clear correlation to the western Caledonian Deformation Front and similar early east-dipping subduction phases in the British Caledonides and Appalachians (Grampian and Taconian phases), suggest that this structure is a fossil eclogitised subduction zone of Caledonian age. Amplitude variations of this upper mantle structure and the Moho conversion further suggest that this fossil subduction zone is accompanied by a partly serpentinitised mantle wedge.

The CF broadband array is closely surrounded by four wide-angle profiles on which the crustal P -wave velocity structure was quantified (Schlindwein & Jokat 1999; Voss & Jokat 2007). These data identified substantially thickened crust reaching more than 40 km in the Caledonian hinterland. Beneath the more distal areas of the study region, Devonian and Mesozoic basins, as well as lower crustal bodies interpreted as magmatic underplating, are observed. Further, Devonian extension in the region is associated with a shallower east dipping shear zone and a west dipping lower crustal detachment zone, which might have produced a considerable Moho offset between thick crust in the west and thin crust in the east (Schlindwein & Jokat 2000). However, deeper structures were not identified, probably due to the limits of resolution of this method.

The evidence from different published gravity, seismic and receiver function studies show similar results, but there are also some differences. Details of the crustal and upper mantle structure are crucial to understand Caledonian evolution, especially in light of recent findings. Of central importance is the question whether or not a fossil Caledonian subduction zone is in place, and if the mantle wedge and lower crustal bodies are of an igneous nature or represent serpentinitised/hydrated mantle peridotite. These issues have an impact on interpretations of the post-Caledonian evolution and the isostatic state of the crust and lithosphere.

3 RECEIVER FUNCTION ANALYSIS

P -to- S receiver functions were estimated from the waveforms of the CF array in order to isolate conversions of teleseismic P to S waves at velocity discontinuities beneath each station (Langston 1979; Ammon 1991; Kind *et al.* 1995; Bostock 1998). The two horizontal components of the three recorded waveforms (north, east

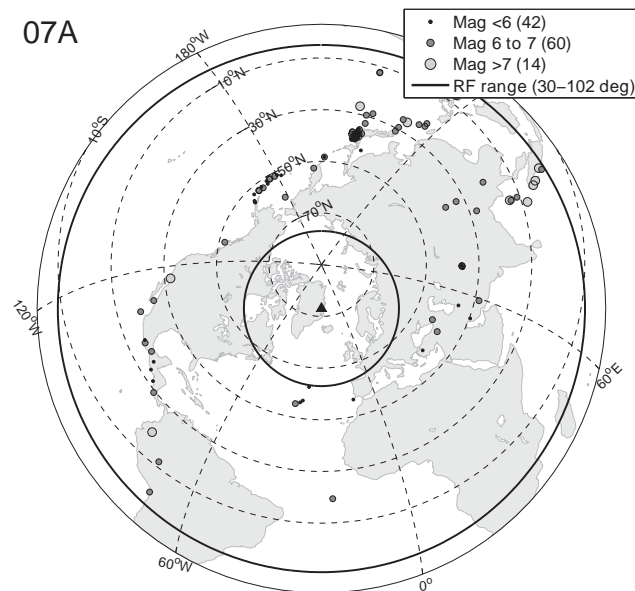


Figure 3. Locations of finally processed events at station 07A. The chosen maximum amount of events at station 07A, at which most events were used, divided into magnitudes <6 (small black circle), 6–7 (medium dark grey circle) and >7 (large light grey circle). Black triangle indicates the location of the station. Large black circles indicate the epicentral distance range for receiver function modelling.

and vertical) were initially rotated into the direction of the incident earthquake wave creating the R - and T -components (radial and transversal). Further vertical rotation by the incidence angle of the wave was applied in the R - Z -plane, which separates effects of P and S wave on the theoretical L - and Q -components, respectively (Vinnik 1977). After a spectral whitening of the signals, we applied the ‘waterlevel’ deconvolution (Clayton & Wiggins 1976; Langston 1979; Ammon 1991), thus removing the Z waveform from the R component (or L from Q). This procedure aims to eliminate the teleseismic wavelet from the signals including the earthquake source effects, the instrument response and several other effects on the teleseismic ray path, thus creating R receiver functions (or Q receiver functions). The remaining signals are ideally dominated by the isolated P -to- S conversions in time and were smoothed with a Gaussian filter of a Gaussian parameter of 2.5. The difference between R -RFs and Q -RFs is that R -RFs show a fraction of the incoming P -wave signal, whereas this was removed in Q -RFs, which allows a clearer view on the conversions only.

3.1 Data and quality

Locations of the events used at each station are shown in Fig. 3 (station 07A) and Fig. A1 (all other stations). Piercing points of all the events in the region at the base of a homogeneous layer of 40 km thickness with a P -wave velocity (V_p) of 6.4 km s^{-1} and S -wave velocity (V_s) of 3.7 km s^{-1} can be seen in Fig. 4 that illustrates the general ray-coverage.

Receiver functions computed from all events with a magnitude over 5.5 were selected for later modelling based on the following noise level criterion. Ideally, any receiver function should be zero at negative times. We took the root-mean-square noise level of the receiver function for times before $t = 0$ as a pragmatic quality measure from which we ranked the receiver functions from ‘best’

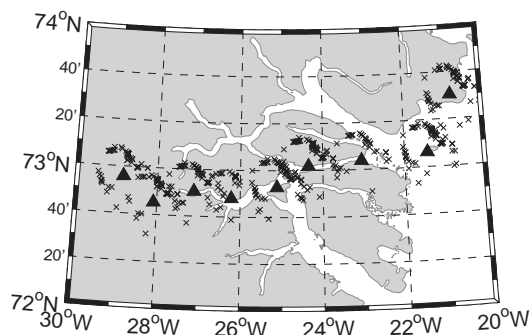


Figure 4. Piercing points of all the events used in this study at the base of a 40-km-thick layer with a homogeneous V_p of 6.4 km s^{-1} and V_s of 3.7 km s^{-1} .

to ‘poorest’. Fig. 5 shows the stacks resulting from the ‘best third’, the ‘intermediate third’ and the ‘poorest third’ for all stations. The rms values of the R -RF amplitudes before $t = 0$ range from 0.013 to 0.023 for the ‘best third’ to 0.020–0.047 for the ‘poorest third’ (see Table 1). Based on this analysis of the ranked receiver functions only the best 30–70 per cent of the receiver functions seem to be of reasonable quality. This criterion was slightly violated at stations 01A and 11A, where more events were selected (65 and 70 per cent, respectively) to ensure a sufficient number of RFs for the stack. From the accepted waveforms a ‘small stack’ and a ‘large stack’

are created. These two stacks were fed into the subsequent inverse modelling in order to assess the stability of the inversion for the given set of events. Table 1 shows the percentiles used in each stack at each station.

3.2 Inverse receiver function modelling

A well-established and fast RF processing method is the common conversion point stacking, which projects each RF along its theoretical teleseismic ray path to the corresponding conversion point in the subsurface, based on a reference velocity model (Bostock 1998; Kosarev *et al.* 1999; Svenningsen *et al.* 2007). This has already been published for this data set (Schiffer *et al.* 2014). This method allows for a better spatial and structural assessment of the subsurface as compared to simple stacking of events (Fig. 5).

Another powerful approach is receiver function inversion of local 1-D models leading to an image of the subsurface velocity structure (e.g. Owens *et al.* 1987; Cassidy & Ellis 1993; Sandvol *et al.* 1998a; Darbyshire 2003; Ottemöller & Midzi 2003). Inversion of RFs is usually regarded as a non-unique problem (Ammon *et al.* 1990), mainly because of multiples that may be modelled as primary conversions and a trade-off between thickness and velocities for corresponding delay times. Also, RFs are sensitive to mainly horizontal S -wave discontinuities, whereas the P -wave velocity structure has less impact on delay times and amplitudes, and the absolute velocities are less well constrained (Sandvol *et al.* 1998b; Julià *et al.*

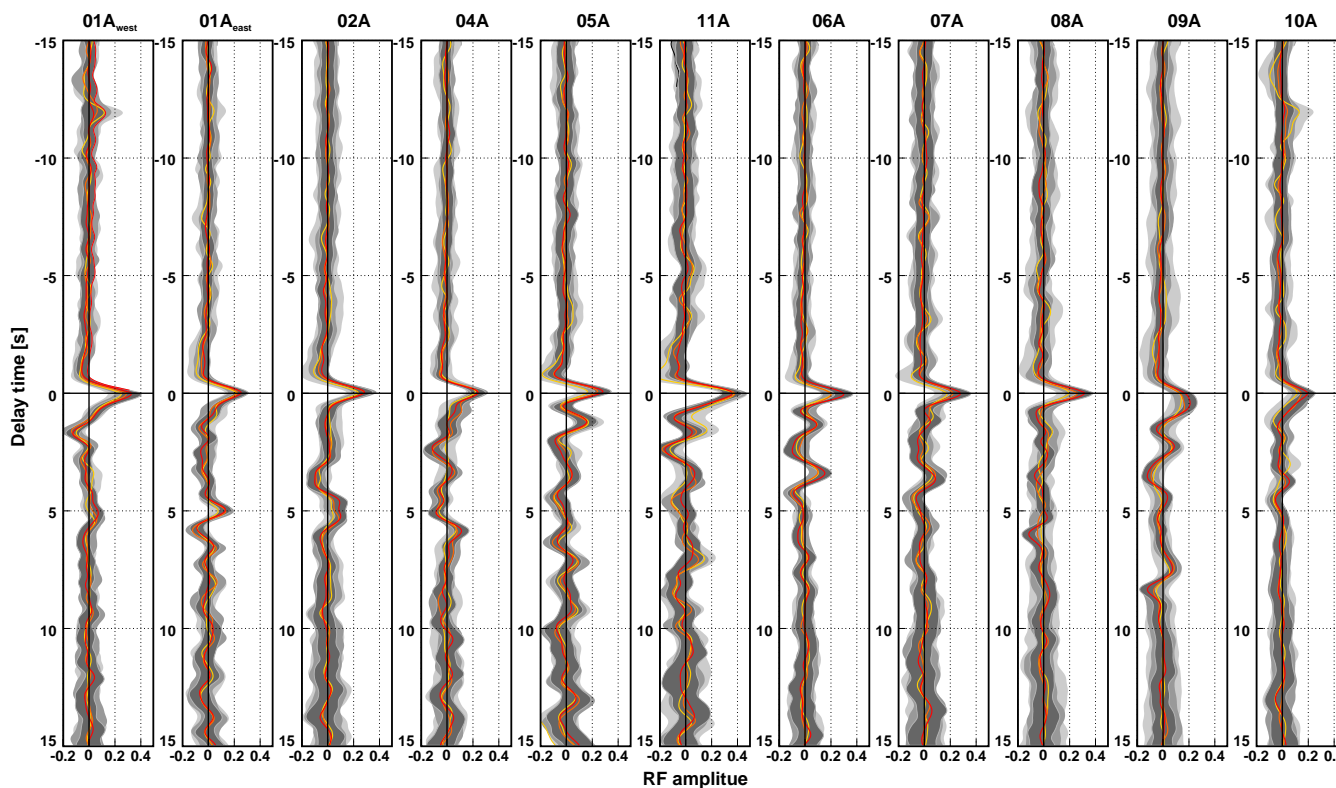


Figure 5. Variability of receiver function stacks. The receiver function stacks (red, orange, yellow) and the standard deviation at each time sample (grey shadings) is shown for different, independent stacks at each station (and backazimuth bins, west-east at station 01A). The three stacks are created from different portions of all accepted events, with regard to the noise level before P -arrival ($t = 0$): Red and dark grey – 33 per cent events of highest quality; orange and middle grey – 33 per cent of average quality; yellow and light grey – 33 per cent events of lowest quality. As would be expected, we generally observed that the ‘noise-level’, represented by the standard deviation increases by stacking ‘noisier’ events. Some stations show an overall better quality (e.g. 01A, 05A, 06A and 09A) than others (e.g. 11A, 07A and 08A). This figure also illustrates the quality of the successively more ‘noisy’ events and thereby gives an idea about where to cut off a stack to ensure good data quality (*cf.* Table 1). For example, station 11A is quite consistent for the stack of the best and second best, but shows a large departure for the ‘worst’ stack.

Table 1. Station information and amount of used events in the RF stacks and inversion. The inversion is performed for two different stacks of the receiver functions available at each station. The percentile and thus number of events largely depends on the quality of the station. The rms of the noise amplitude (RMS_{amp}) is shown for stacks of the best, intermediate and poorest third of the events.

	Lat (°)	Long (°)	Elevation (m)	Instrument	RMS_{amp}			Stack 1		Stack 2	
								per cent	N	per cent	N
01A_{west}	72.930	−28.830	1524	Güralp 3TD	0.020	0.023	0.038	40	16	65	23
01A_{east}					0.016	0.019	0.029	40	36	65	50
02A	72.755	−28.082	1047	Güralp 3EX	0.015	0.018	0.025	25	47	50	72
04A	72.844	−27.115	1110	Güralp 3TD	0.015	0.015	0.022	35	45	60	63
05A	72.798	−26.213	1115	Güralp 3TD/3EX ^a	0.017	0.017	0.032	25	33	50	53
06A	72.880	−25.118	36	Güralp 3TD	0.013	0.016	0.020	45	51	70	65
07A	73.030	−24.351	90	Güralp 3TD	0.015	0.020	0.022	45	82	70	116
08A	73.065	−23.057	55	Güralp 3TD	0.015	0.018	0.027	25	22	50	34
09A	73.104	−21.437	127	Güralp 3TD	0.015	0.020	0.027	25	45	50	80
10A	73.503	−20.805	193	Güralp 3TD	0.016	0.025	0.045	25	37	50	69
11A	73.274	−26.452	1260	Güralp 3EX	0.023	0.029	0.047	45	39	70	50

^aExchange of instrument during maintenance in summer 2010.

2000; Zhu & Kanamori 2000). Other seismological constraints on absolute V_s are therefore often jointly inverted together with RFs in order to add more stability to the estimation of realistic models. Examples are the inversion of surface waves (Du & Foulger 1999; Julià *et al.* 2000) or the apparent S -wave velocity information of receiver functions (Svenningsen & Jacobsen 2007).

A fairly standard linearised least-squares inverse approach was applied in order to obtain crustal and upper mantle velocity models (Tarantola & Valette 1982; Menke 1989; Ammon *et al.* 1990). The vector of free parameters included S -wave velocities and the vertical extents of the layers. We chose to parameterise the vertical extent by the seismic delay times instead of the more commonly used thickness. This parameterisation dramatically enhances the uniqueness and linearity of the receiver function inversion implying fast convergence, almost independent of the starting model (Jacobsen & Svenningsen 2008). Our inversion setup minimises the total cost function

$$Q_{\text{tot}} = Q_d + Q_p = (d_{\text{obs}} - Q_{\text{mod}})^T \cdot C_d^{-1} \cdot (d_{\text{obs}} - d_{\text{mod}})^1 + (p_{\text{prior}} - p_{\text{mod}})^T \cdot C_p^{-1} \cdot (p_{\text{prior}} - p_{\text{mod}})^1, \quad (1)$$

where the ‘data misfit’ Q_d and ‘prior penalty’ Q_p are computed from observed data d_{obs} , modelled data Q_{mod} , an observed data error covariance matrix C_d (assumed to be diagonal), a prior model parameter vector p_{prior} , assumed errors of the prior model C_p (also assumed diagonal) and a final, modelled parameter vector p_{mod} .

As good surface wave coverage is missing, we employed the $V_{s_{\text{app}}}$ method (Svenningsen & Jacobsen 2007). The ratio of R -RF to Z -RF at zero delay time (R - Z ratio) may be shown to resolve the absolute S -velocity near the surface of a homogeneous medium (Wiechert & Zoeppritz 1907). When a given RF is smoothed by a Gaussian filter of width T we may compute an apparent half space velocity $V_{s_{\text{app}}}(T)$. As this smoothing width is increased, the apparent S -velocity will average the real S -velocity to increasing depths. The $V_{s_{\text{app}}}(T)$ curve therefore enhances the low-frequency information in the receiver function, and Svenningsen & Jacobsen (2007) showed that for adequate quality broadband stations, the $V_{s_{\text{app}}}(T)$ data did define good average S -velocities in the crust and uppermost mantle. We combined the pure $V_{s_{\text{app}}}(T)$ inversion of Svenningsen & Jacobsen (2007) with the conventional fitting of the RFs. Using this procedure we have put some weight on the robust low-frequency information on average S -velocities without losing the interface-resolving power of the receiver function. Since

$V_{s_{\text{app}}}$ curves were computed from the receiver function waveforms, a perfect receiver function fit should obtain a very similar $V_{s_{\text{app}}}$ curve, however, small-scale 2-D/3-D scattering is more likely to produce spurious wiggles and less likely to shift the averaged information in the $V_{s_{\text{app}}}(T)$ data.

The forward mapping implies the estimation of a synthetic RF waveform for an impulsive teleseismic event (Kennett 1983). Because the observed receiver function has a minimised but still significant waveform width and complexity we convolved the synthetic impulsive RF with the observed L -component. This synthetic waveform defines the misfit to the observed RF. From the synthetic RFs a $V_{s_{\text{app}}}$ curve was estimated, which then defined the misfit to the observed $V_{s_{\text{app}}}$ -data.

Following Tarantola & Valette (1982), our inversion also allows prior values and prior uncertainties to model parameters. One important source of prior velocity information is comprised by the P -wave velocity models from wide-angle studies performed in the vicinity of the CF array (Schlindwein & Jokat 1999; Voss & Jokat 2007; Fig. 6 upper panel, red and Fig. 7c). S -wave velocities were calculated using a V_p - V_s ratio curve, based on commonly observed lithologies in the expected velocity ranges (Christensen 1996) and densities from a fixed V_p -density relationship for specific crustal depth ranges (Christensen & Mooney 1995).

To keep the number of parameters as small as possible, we constructed velocity models with as few layers as possible. First, layer main boundaries were defined by initially investigating the receiver function waveforms. At delay times below 6 s, which roughly corresponds to the lowermost limit of a plausible crustal thickness layer, boundaries were defined where major positive receiver function signals were observed. In principle, these signals can be primary but also multiple conversions. However, we expect the inverse model to solve this distinction, since primary conversions should always be accompanied by corresponding multiples. Additional layers were added if necessary to reach data fit. Two layers were defined at delay times of the upper and lower interface of the previously interpreted slab and another layer in the overlying upper mantle, if required. The prior velocity in the presumed slab was set equal to the velocity in the surrounding mantle. Any velocity contrast between slab and mantle will therefore be data driven. During the inversion, all parameters were assigned to be free and only limited by the assigned prior uncertainty that allowed all layer boundaries (parametrised as delay time) as well as the velocities to change. The inversion thus defined the final model parameters such as

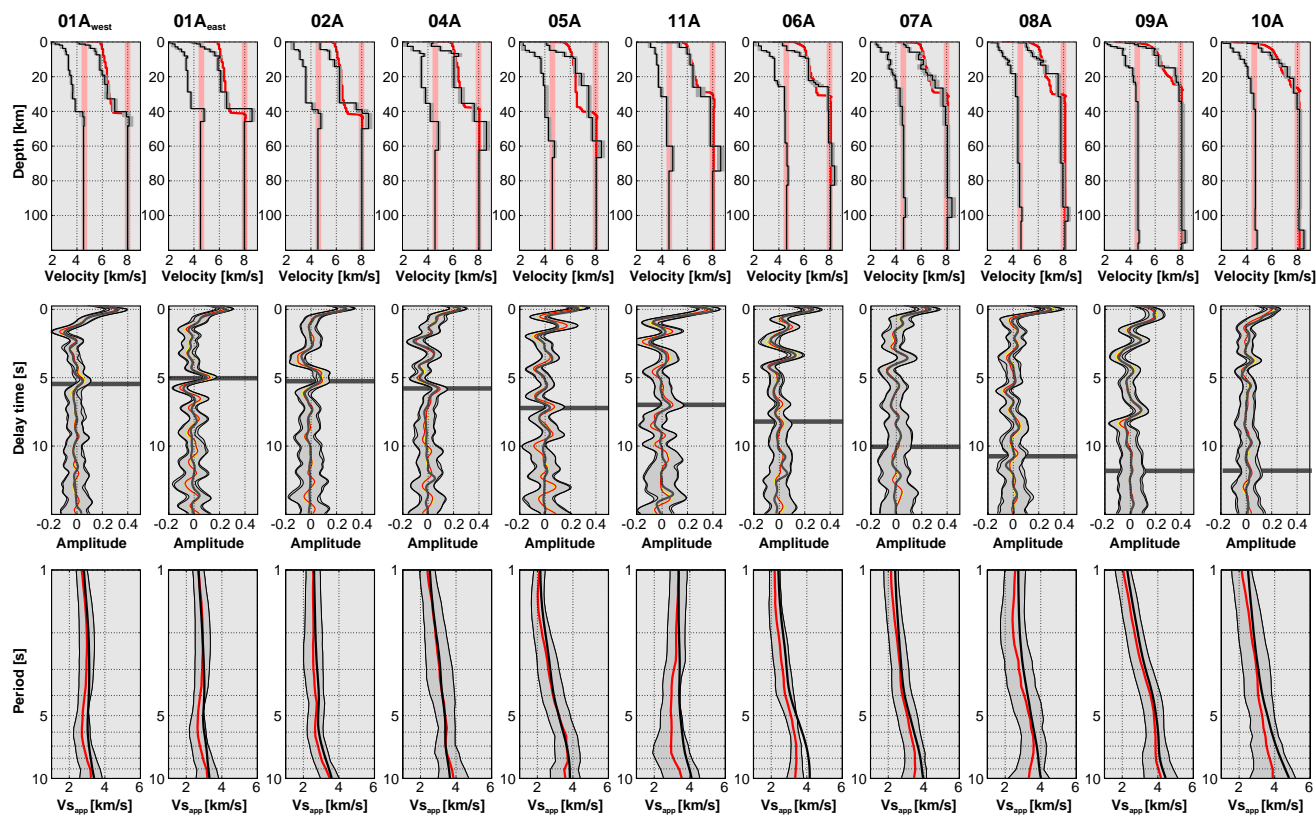


Figure 6. Receiver function inversion showing R–RFs. Upper panel: final V_s and V_p velocities (black) and posterior standard deviation (grey shading, see text). Red is the prior model from wide-angle seismics. Red shading indicates standard mantle velocity of approximately $V_s = 4.6 \text{ km s}^{-1}$ and $V_p = 8.05 \text{ km s}^{-1}$. Middle panel: R-receiver function waveforms. Black – synthetic RF. Yellow – Small fraction stack. Red – large fraction stack. Grey shading – Standard deviation of individual RFs. Dark grey horizontal line – delay time of the modelled upper slab interface. The waveforms of the two different stacking fractions are almost identical. Lower panel: $V_{s_{app}}$ curves. Red – observed (median of all events at one station). Black – synthetic $V_{s_{app}}$ curve.

velocities, but also layer boundaries, which were only initially set up to correspond to possible major conversions.

We performed a number of inversion runs for each station. First, we computed the ‘small stack’ and ‘large stack’ using two different percentiles of the available events (described above, Table 1), which did not show a considerable variation of the resulting models (Fig. 6 middle panel, yellow and red). The chosen amount of data depended on the recording time of each station and the data quality. For these two data subsets, an inversion was performed for the stacked R–RFs (Fig. 6) and Q –RFs (Fig. A2), leading to almost identical models at each station. We tested highly different starting models, but the resulting inversions were also almost identical. Although the differences of all performed RF inversions at each station were negligible, we defined the mean model as the final model result (Fig. 6, upper panel and Fig. A2). The posterior parameter error in this case is estimated by the diagonal of the posterior covariance matrix $C'_p = (G^T \cdot C_d^{-1} \cdot G + C_p^{-1})^{-1}$ (G is the Jacobian matrix of partial derivatives of the forward function; C_d and C_p explained above).

3.3 Receiver function results

The obtained RFs indicate a complex structure beneath the CF region of East Greenland. The CF array crosses the study area at $\sim 73^\circ\text{N}$ on an approximately west–east oriented profile, roughly perpendicular to the exposed Caledonian orogenic and post-Caledonian extensional structures (Fig. 2). The stations in the western half of the array are located on top of gneisses, Palaeozoic sediments

and metasediments (01A–05A and 11A), whereas the eastern stations are situated on top of younger, Devonian–Mesozoic sediments (06A–08A). The two easternmost stations (09A and 10A) lie on top of Tertiary flood basalts. The $V_{s_{app}}$ curves reflect this west–east variation (Fig. 6, lower panel). Whereas the western stations show S -wave velocities of approximately 3 km s^{-1} and higher at 1 s (with one exception of 2.1 km s^{-1} at 05A), the easternmost stations show much lower velocities of 2 – 2.5 km s^{-1} . As an effect of the RFs and $V_{s_{app}}$ curves, the inverse models also show a significant change in velocities from station 06A and westward, the area where the Devonian and post-Caledonian basins occur. Almost all stations show a thin uppermost layer of low velocities and a steep gradient in the RF inversion (Fig. 6, upper panel), also in the west.

In order to identify the Moho conversion, the sensitivity of RFs to the vertical S -wave velocity structure, mainly—and less to P -wave velocities—must be considered. Hence, prior constraints on the V_p – V_s ratios—as employed in this study—might bias the V_p structure, whereas V_s can be regarded as a generally more robust estimate. Some stations show a clear Moho conversion, which accounts for stations 01A–07A and 11A. The three easternmost stations (08A–10A) show very complex signals. 08A seems to lack strong crustal conversions, including Moho. The inversion indeed shows a very gradual structure and a weakly expressed Moho in order to account for that. Here it is uncertain whether this represents high-velocity and possibly intruded mafic lower crust, or if this is already part of the upper mantle. This applies also for stations 09A and 10A which both show a gradual transition from crustal to mantle velocities. Station 09A (and the eastern events of 08A) shows a strong negative

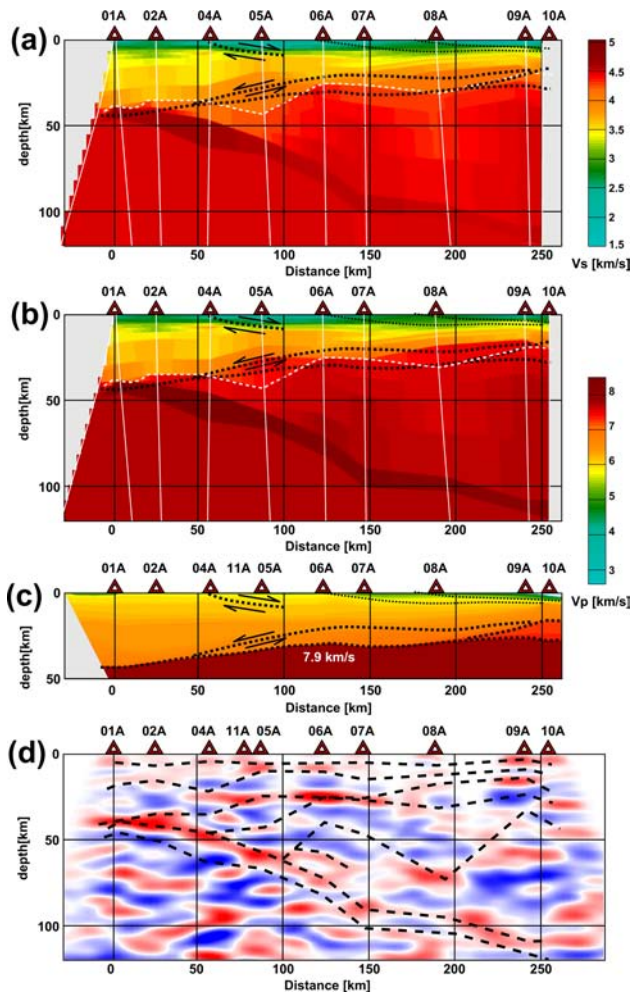


Figure 7. Results from receiver function modelling. (a) S -wave velocity model with our Moho interpretation (white stippled line) and superimposed tectonic structures and Moho from interpreted wide-angle seismics (Schlindwein & Jokat 2000). (b) Same as (a) but with P -wave velocity model. (c) P -wave model from interpolation between wide-angle seismic profiles in the region (Schlindwein & Jokat 1999; Voss & Jokat 2007). (d) Updated RF CCP stacking image with superimposed major velocity discontinuities from the obtained inverse models (stippled lines).

conversion at delay times where the Moho could usually be expected for the stations to the west (Fig. 7d). Being explained as strong, negative multiples from intra-crustal or sedimentary discontinuities it was convincingly modelled as such. The same can be observed at 10A, but at slightly greater depth. Stations 09A and 10A show the lowest uppermost velocities of all stations in the array.

The RF inversion constrains considerably lower V_p in the uppermost 10 km compared to previous estimates from wide-angle seismics (Schlindwein & Jokat 1999; Voss & Jokat 2007). This might partly be caused by methodological differences in resolution and sensitivity. Uncertainty may be caused by the marine-land interaction during the seismic data acquisition and the applied assumptions for its correction during data processing. Another possibility is that V_p - V_s ratios for sedimentary materials were underestimated in the RF modelling. Low S -wave velocities could be an effect of the texture of the rock (e.g. by crustal scale fracturing), which might affect V_s more than V_p . If a too low V_p - V_s ratio was assumed for these velocity ranges the result would be a too low V_p as compared to the absolute V_p estimates from the wide-angle studies.

As mentioned above, at almost all stations (except for station 01A) a zone of ‘intermediate’ velocities, which are too high for normal crust and too low for normal mantle, is observed. This zone is located below velocities that can clearly be assigned to normal crust and shows considerable variation in velocities and thickness (Figs 6 and 7). A 9–18-km-thick high-velocity layer, showing V_s from approximately 4.6–4.8 km s⁻¹ and V_p from 8.3 to 8.7 km s⁻¹ has been estimated to underlie the zone of intermediate to mantle velocities at all stations, except for station 01A. Here, it seems to directly underlie normal crust of approximately 40 km thickness and is not resolved to the west of station 01A. This high-velocity layer dips to the east and reaches a depth of ~90 km in the centre of the array (station 07A), after which the angle of dip decreases. In the eastern end of the array the high velocity layer reaches a depth of ~110 km (Figs 6 and 7). The depth of the upper and lower interface of the slab from RF inversion coincides well with positive (red) and negative (blue) conversions in the CCP image (Fig. 7d). The associated conversion might appear less clearly in the RFs (both stacks and CCP) because crustal multiples may interfere with primary conversions at these delay time ranges (~8–12 seconds). As discussed above, we believe that the receiver function inversion can model primary and multiple conversions well enough so that the estimated slab geometry is a robust feature.

This complexity in the crust and upper mantle is not observed in previous models from wide-angle studies that obviously lack the upper mantle high-velocity layer (Schlindwein & Jokat 1999; Voss & Jokat 2007). Despite the differences, similarities can also be noted, such as the general trend and amplitude of the crustal thickness as well as the occurrence of anomalous lower crustal bodies at the base of ‘normal’ crust (Fig. 7). The lower crustal body imaged in the wide-angle data corresponds very well in velocity and depth with the structures of ‘intermediate’ velocities in the RFs. The receiver functions seem to map this structure further to the west. Also, the wide-angle data obtain a slightly lower mantle velocity of 7.9 km s⁻¹, which is still not as low as the receiver function estimates in the mantle wedge between high-velocity slab and the crust.

The receiver function inversion is in accordance with what was previously interpreted as an east-dipping fossil subduction zone from receiver function common-conversion-point imaging (Schiffner *et al.* 2014) and also shows general agreement with the crustal velocities of wide-angle data.

4 GRAVITY AND ISOSTASY

Because of a general correlation between seismic velocities and densities it is relevant to use gravity and isostatic calculations to test the regional variation in the crust and upper mantle that was obtained by the receiver functions. More specifically, we worked with a 2-D density structure under the CF array, using the program system IGMAS+ (Schmidt *et al.* 2010).

Gravity data were extracted from a compilation for the Arctic region, ArcGP (Forsberg & Kenyon 2004; Kenyon *et al.* 2008). ArcGP consists of measurements previously compiled in the DTU10 gravity model (Forsberg 1986; Andersen *et al.* 2009). The Bouguer anomaly in this data set is obtained using a simple Bouguer plate correction for the topography with a density of 2670 kg m⁻³ except for the ice coverage where a density of 970 kg m⁻³ was applied (Gaina *et al.* 2011). The data set is, however, not terrain-corrected and we assume that the lack of terrain correction may represent errors of up to 30 mGal in rough terrain, such as along fjord edges

(Schmidt-Aursch & Jokat 2005). This error (always slightly underestimated values) will affect short wavelengths (<25 km) only, whereas the regional trend can be regarded as a robust feature.

For the present 2-D regional assessment of the gravity field, we computed the latitudinal average Bouguer anomaly over a distance of 50 km (25 km to the north and south) along the profile (Fig. 8). Through this averaging, the missing terrain correction will diminish, but we still consider possible errors of 10–20 mGal in the gravity data. The gravity field shows a large variation along the approximately 255 km profile between circa –200 mGal at the western end and +50 mGal at the eastern end. The central part shows a flat plateau-like gravity field of circa –50 mGal over a distance of 75 km. The same averaging is conducted for the topography. At the western end of the profile bedrock topography reaches a maximum of approximately 1700 m and gradually decreases to approximately 200 m close to the coast. The profile is for the most part ice-free and only in the western margin covered by 100–200 m of ice. The topography remains close to sea level before dipping steeply down at the continent-ocean transition ~150 km east of the coast. Further to the west, outside the coverage of the CF array, the thickness of the ice sheet quickly increases to two kilometres and more.

A simple first order test was performed as follows. We chose the Nafe-Drake V_p -density relation to obtain a first density model directly from the V_p model in Fig. 7(b). The gravity response of this model was in good agreement with the observed data (Fig. 9). The ‘direct’ response of the RF model is generally too smooth and shows an almost linear gradient of 300 mGal over the 255 km of the CF array. For example, the model is not able to explain the area of almost constant Bouguer anomaly of circa –75 mGal at 100–175 km distance and, hence, the flanks do not show the observed steep gradient. Despite all modelling uncertainties, model interpolation and the simple translation from V_p to densities, this test shows that the obtained velocity structure is able to describe the relative gravity field quite satisfactorily and without adjusting the model. The gravity field shows too low values at 50–100 km distance, where the interpreted crust is thick (43.5 km—Fig. 7 at ~90 km distance). If the crust was thinner, the resulting Bouguer anomaly would be higher. On the other hand, the Bouguer anomaly shows too high values for the entire eastern half of the profile. Contrary to the situation to the west, the crust here could be modelled too thin, or the mantle wedge could consist of even lower densities in order to obtain a lower Bouguer anomaly. The density profile is a rather coarse representation of the subsurface as a result of quite large distances between the seismological stations. Variations may exist between the stations which are not represented by the interpolated structure. The Bouguer anomaly response of the obtained crustal structure only (the crust is defined by densities <3100 kg m⁻³, Fig. 9c, black lines) on top of a homogeneous mantle of 3300 kg m⁻³, shows a markedly worse fit. The regional gradient is expressed much more strongly and spans more than 375 mGal from the western to the eastern end of the section (compared to 300 mGal including the complex mantle).

The topographic isostatic response, assuming simple local isostasy, was calculated with regard to the crustal structure (Fig. 9a, stippled red lines) and the complete density model (Fig. 9a, solid red lines). The reference model used to balance the density model was defined as follows: (i) 5 km of water; (ii) 5.6-km-thick oceanic crust (iii) homogeneous mantle to the reference level of 120 km (Turcotte & Schubert 2002). Densities were assigned as described above. The model density structure was averaged over a 50 km wide laterally moving window. As previously conducted, the Moho and thereby the lower limit for the calculation of the crustal isostasy

was defined by a density threshold of 3100 kg m⁻³ (Fig. 9c, black lines). The crust alone is clearly lacking sufficient buoyancy in the east of the section, corresponding to up to 2 km of missing topography. However, the full density structure produces a very good fit. In the west the topography seems to be slightly overcompensated and mainly supported by the buoyancy of the crust. In the east, the topography clearly requires additional support from the buoyant subcrustal lithospheric structure.

5 DISCUSSION

Receiver function modelling in the CF region revealed considerable complexity in the upper mantle, including an eastwards dipping high-velocity slab and a mantle wedge of low mantle velocities (or crust of high velocities). The obtained geometry and velocity structure is generally consistent with the observed gravity field and topography. The crust alone produces a much more inferior fit for both data sets as compared to the entire structure.

5.1 Topography and isostasy

The nature of the passive margins of the NAR is a matter of significant debate including age, origin and state of isostatic compensation. Is the high-elevation, low-relief landscape, which characterises these margins in many places, the product of recently uplifted peneplains, or is it the consequence of climatically controlled slow erosion of old, Caledonian topography as outlined in the geological background section? The simple forward gravity and isostatic test presented here suggests that the lithosphere in the CF region is in a state of near-local isostasy, and that large dynamic topography support is therefore not required. In the east, the density structure of both the crust and the mantle wedge is required to explain the observed topography. In the west, the >40-km-thick crust can account for the entire support of the topography. The root mean square error of the calculated isostatic topography with the observed topography is 277 m. Altogether, this suggests that no pronounced (>300 m) present-day dynamic support is needed to explain the topography in this part of the East Greenland Caledonides.

5.2 Petrology

The seismological signature of the crust and upper mantle in the CF region does not allow a detailed petrological interpretation, but after revisiting Anderson (2007), Christensen & Mooney (1995) or Christensen (1996) the seismic velocities can be brought into a qualitative context for some possible compositions. Values for V_p of 7.3–7.8 km s⁻¹ and V_s of 4.0–4.4 km s⁻¹ in the mantle are consistent with a number of different compositions. Hydrated and partly serpentinised mantle peridotite, mafic and partly eclogitised lower crust as well as intruded mafic lower crust could account for the estimated velocity ranges. ‘Dry’, for example pyroxene rich mantle compositions can, in theory, also show seismic velocities of down to $V_p \approx 7.7$ ($V_s \approx 4.4$), which is only the upper limit of the observed velocities in the mantle wedge. The presence of melts which could reduce the seismic wave speed is not considered because of the complete absence of present-day active volcanism in the Central Fjord Region.

The high velocities associated with the dipping structure could be explained by eclogitised mafic crust. This could explain the apparent velocity drop below the shallower velocity increase and thereby define a distinct, thin high-velocity zone. The presence of a

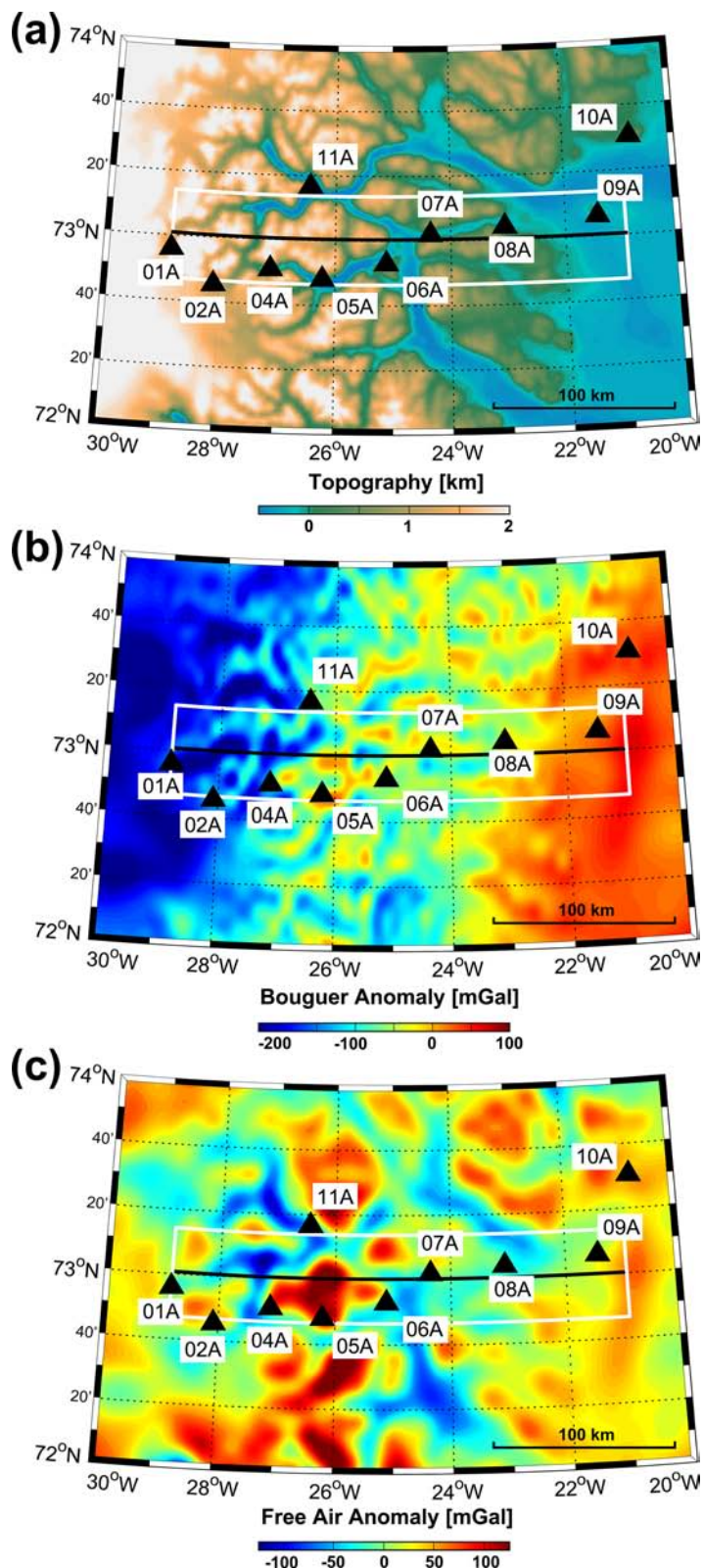


Figure 8. Topography and gravity data in the Central Fjord region. Black triangles – station locations. Stippled black line – position of the section for gravity and seismicological modelling. (a) Topography, (b) Bouguer anomaly and (c) free air anomaly (gravity data from the Arctic data compilation ArcGP (Forsberg & Kenyon 2004; Kenyon *et al.* 2008)). For the Bouguer gravity a local correlation with topography is due to the lacking terrain correction. In the free air anomaly we observe the fjords and local topographic features standing prominent negative and positive gravity anomalies, respectively, demonstrating isostatic disequilibrium of these small-scale structures.

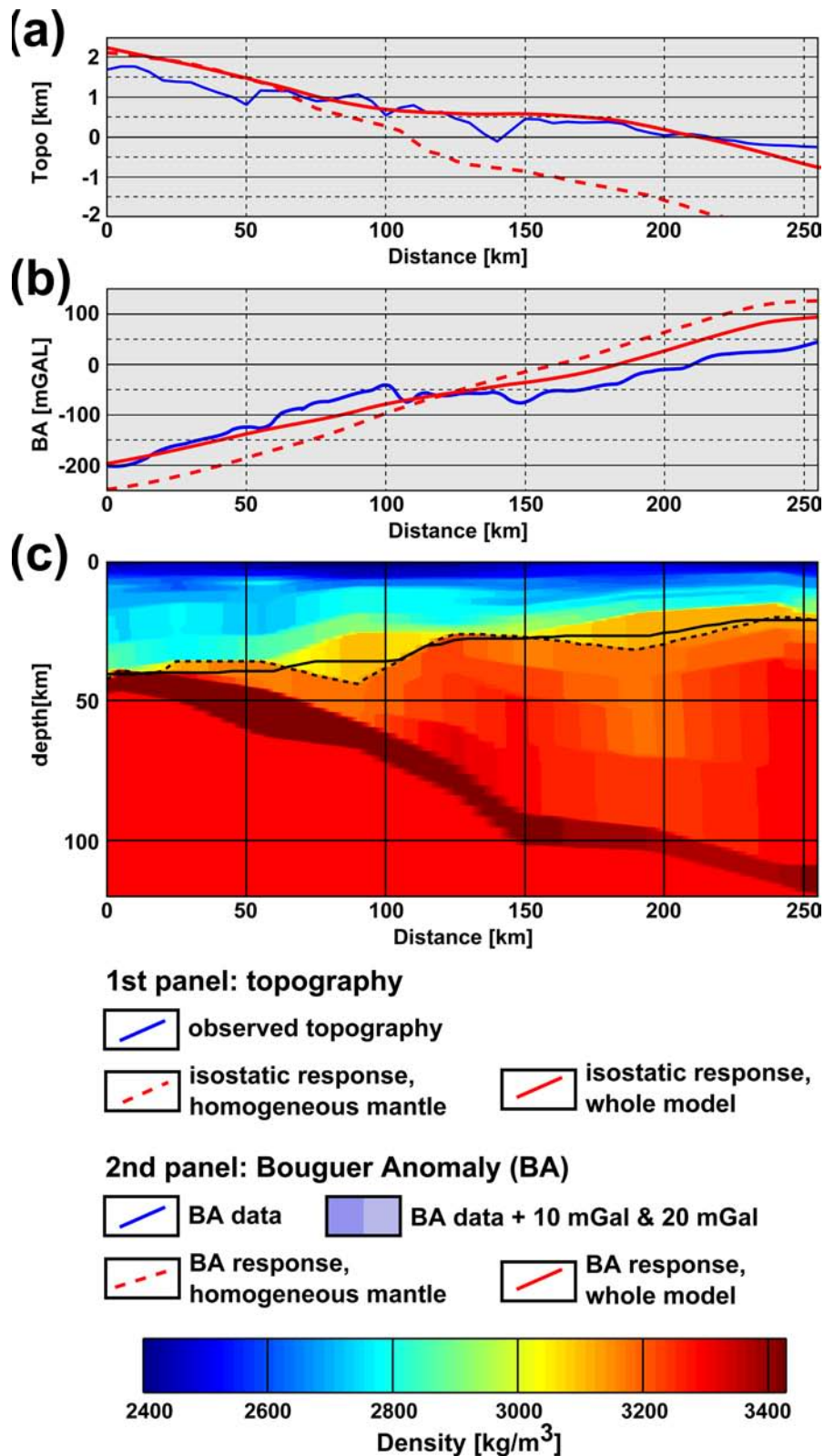


Figure 9. Results from gravity and isostatic modelling. (a) Topography observed (blue) and isostatic response of the crust (stippled red) and the whole lithosphere (solid red). (b) Bouguer anomaly; observed (blue) and response of the entire model (solid red) and of the crustal model with a homogeneous mantle of density 3300 kg m^{-3} (stippled red). Blue shading indicates the BA data plus 10 and 20 mGal to illustrate the possible terrain correction error. (c) Density model of the section (same as seismology section in Fig. 7), stippled black line: Moho interpretation ($\rho < 3100 \text{ kg m}^{-3}$); solid black line: Moho interpretation averaged over a 50-km-wide moving window.

high velocity, garnet and/or iron rich mantle does not make sense in such a thin and well-confined slab, but such a mantle composition could explain the velocity increase at the upper interface of the slab. The lower velocity drop could be temperature-induced, but we speculate that this would probably be insufficient to explain the observations.

Of all mentioned possibilities, the most plausible may be a fossil subduction zone setting, including a slab of eclogitised mafic crust and a mantle wedge of variably hydrated and serpentinised mantle peridotite. Mantle hydration and partial serpentinisation can explain the observed low-velocity mantle wedge, possibly enhanced by a different mantle composition of an accreted terrane. The lowermost crust and uppermost mantle layer may represent a zone of lower crustal bodies of intruded mafic material, possibly chemically and physically mixed with serpentinised mantle peridotite.

Igneous (White 1992; Menzies *et al.* 2002) and serpentinite (Olafsson *et al.* 1992; Mjelde *et al.* 2002; Osmundsen & Ebbing 2008) but also metamorphic (Gernigon *et al.* 2004; Gernigon *et al.* 2006; Mjelde *et al.* 2013; Kvarven *et al.* 2014; Nirrengarten *et al.* 2014) origins have been invoked to explain lower crustal bodies at passive margins. A possible igneous component might be the consequence of arc-magmatism in a subduction setting or igneous activity due to continental break-up. Break-up related intrusions have previously been suggested in the study area (Schlindwein & Jokat 1999, 2000; Voss & Jokat 2007; Voss *et al.* 2009).

Mantle hydration and serpentinisation of the upper mantle can occur by two mechanisms: Either *in situ* hydration through cracks in extremely thinned crust (Manatschal *et al.* 2001; Pérez-Gussinyé *et al.* 2003), or subduction of water into the upper mantle (Peacock 1993; Iwamori 1998; Bostock *et al.* 2002; Hattori & Guillot 2003; Hyndman & Peacock 2003; Duesterhoeft *et al.* 2014). The serpentinite stability limit for realistic P-T conditions (Ulmer & Trommsdorff 1995) is at about 50–60 km depth or more (Duesterhoeft *et al.* 2014; Guillot *et al.* 2015). At higher temperatures, metamorphosed serpentinite will still show lower densities and velocities (Duesterhoeft *et al.* 2014).

We suggest that the lower crustal bodies in the eastern end and further east might be dominated by break-up related intrusions. In contrast, the lower crustal bodies in the central and western part of the CF array could represent a combination of arc-magmatic intrusions, mildly metamorphosed crust and partially serpentinised mantle peridotite.

5.3 Tectonic evolution

Given this qualitative petrological assessment, our preferred model includes a Caledonian, east-directed subduction event. Most likely, the colliding block from the east was a continental terrane of Laurentian affinity. The slab geometry appears to flatten out at a depth of 100 km and shows similarities to an observed fossil subduction zone in northwestern Canada (Mercier *et al.* 2008; Queyfe & Clowes 2010). We identify two possible explanations for this behaviour. First, crust could have subducted in a flat subduction setting, and secondly, the geometry could be caused by deformation and lithospheric thinning during subsequent extension and continental break-up.

We suggest initial oceanic subduction, followed by continental underthrusting, indicated by thicknesses of up to 18 km for the shallow part of the slab. The subduction could have terminated due to buoyant resistance of the continental crust. Subduction of more buoyant crust, due to continental fragments or oceanic plateaus,

has been suggested to cause flat subduction modes (Gutscher *et al.* 2000b; van Hunen *et al.* 2002, 2004). Slab and mantle wedge melting is usually initiated at a depth of around 100 km, also in flat subduction settings (Gutscher *et al.* 2000a). This is in excellent agreement with the relative location of the imaged slab and lower crustal bodies.

The above was followed by the Scandian phase, during which Baltica was underthrust west beneath Laurentia with flipped subduction polarity. The location of this subduction and the main collision zone would have been situated further east at sufficient distance from the Laurentian margin to preserve the early eastward subduction zone complex. Accreted terranes of sufficient width might have provided a buffer zone, preventing the Scandian deformation from continuing to the west.

After their formation, the Caledonides experienced gravitational collapse, erosion and a slow thinning of the lithosphere. More active rifting took over, culminating in the Palaeocene–Early Eocene continental break up and accompanying magmatism. Because of lithospheric thinning during this long phase of extension, the slab might have been bent up, causing the observed flattening, as an alternative or additional mechanism to the flat subduction model. The apparent preservation and only minor deformation of the slab in contrast to the severely deformed and thinned crust might have been facilitated by a decoupling of crust and mantle lithosphere through a lower crustal west-dipping detachment zone (Schlindwein & Jokat 2000; Fig. 10). Also, the hydrated and partially serpentinised mantle wedge and its ‘soft’ rheology (Hilairiet *et al.* 2007; Reynard 2013; Guillot *et al.* 2015) could have accommodated this decoupling. During time of break-up, lower crustal intrusions were emplaced in the more distal parts of the passive margin (Voss *et al.* 2009).

5.4 Possible bias from anisotropy and lateral inhomogeneity

Anisotropy and deviations from horizontal layering may obviously add some complexity to the conversions and ray paths of incident teleseismic waves (Cassidy 1992; Frederiksen & Bostock 2000; Eckhardt & Rabbel 2011; Schulte-Pelkum & Mahan 2014). This has been analysed in several active and fossil subduction settings. Serpentinised mantle has been found to be anisotropic (Ji *et al.* 2013; Shao *et al.* 2014) and a common feature in mantle wedges and detachment zones (Park 2004; Nikulin *et al.* 2009). Also, mantle fabrics close to the subduction channel may be anisotropic as an effect of the subduction process or frozen-in mantle flow and spreading patterns (Mercier *et al.* 2008; Song & Kim 2011; Audet 2013). In contrast, eclogite is typically much less anisotropic (Worthington *et al.* 2013). Dipping layer geometries cause some variations with azimuth (Frederiksen & Bostock 2000). All these effects are likely to be present in the study area of this paper. Our stacking of receiver functions does average out some of these effects. Still, we cannot rule some bias of the average interval velocities due to a predominant azimuth of the used earthquakes, which come out of our RF modelling. The geometry of bodies and interfaces can be regarded as a more robust feature, because these are resolved by travel times which are much less influenced by anisotropy.

6 CONCLUSION

Inverse modelling of receiver function waveforms shows that the Central Fjord region of East Greenland comprises anomalous crustal and upper mantle geology. The results indicate a high-velocity slab

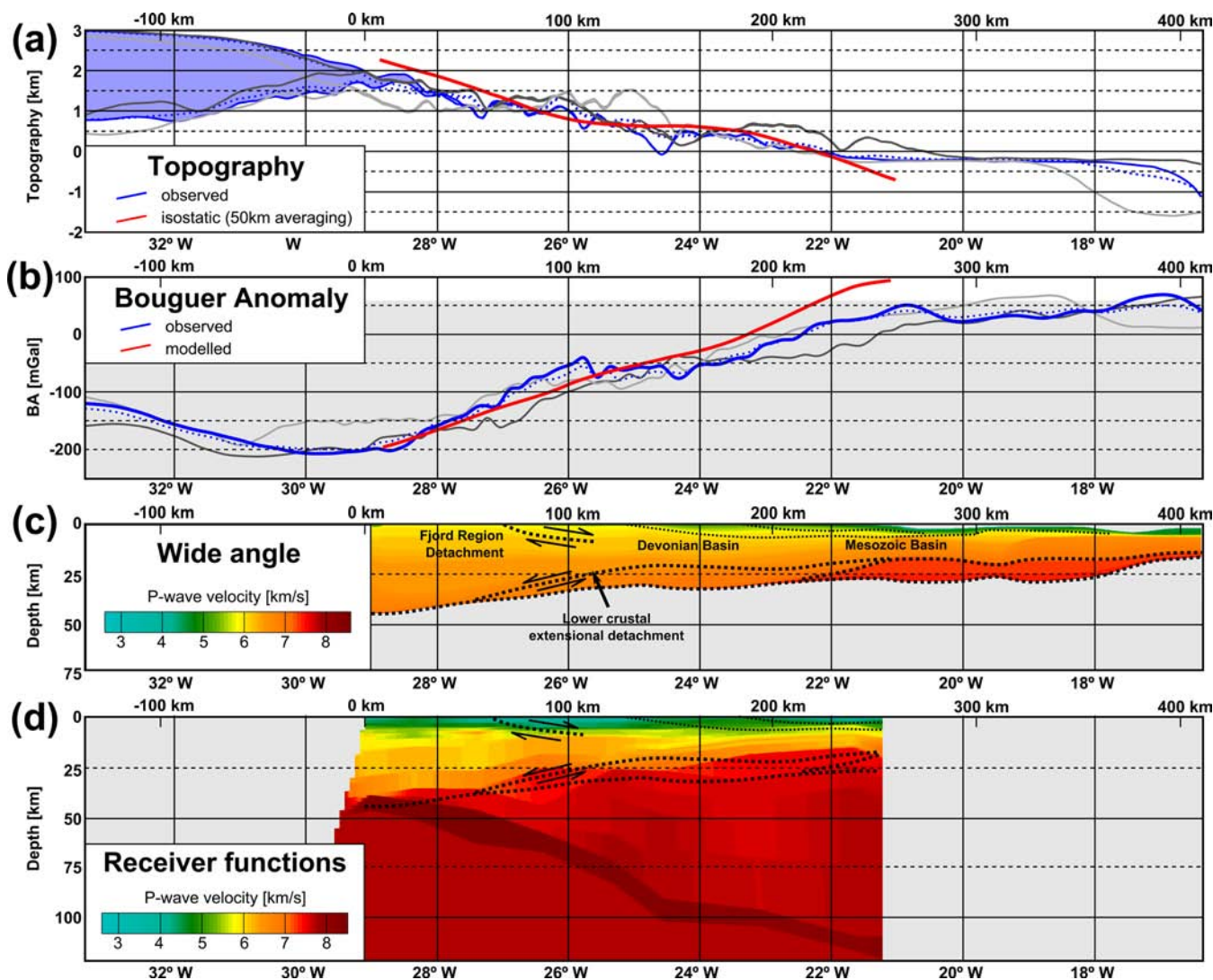


Figure 10. Summary of the preferred interpretations and modelling results. (a) Topography. Blue – observed topography (50 km latitudinal average). Shaded blue area indicates the ice thickness. Stippled blue line – observed topography (100 km latitudinal average). Light grey – 50 km average topography south of the study profile. Dark grey line – 50 km average topography north of the study profile. Upper lines indicates ice topography, lower lines indicates bedrock topography. Red: modelled isostatic topography using a running window of 50 km width to average the lithospheric density structure illustrated in Fig. 9. (b) Bouguer anomaly (BA). Blue line: observed BA (50 km latitudinal average). Dotted blue line – observed BA (100 km latitudinal average). Light grey line: 50 km averaged BA, south of the profile. Dark grey line: 50 km averaged BA north of the study profile. Red: modelled BA from the lithospheric density structure illustrated in Fig. 9. (c) *P*-wave velocity model from wide-angle seismic surveys (Schlindwein & Jokat 1999; Voss & Jokat 2007) and interpolated onto the CF array profile. Crustal tectonic interpretations are from Schlindwein & Jokat (2000). (d) *P*-wave velocity model obtained by RF inversion of the CF array data. Tectonic features as in Figs 7(a)–(c) and 10(c).

($V_p > 8.3 \text{ km s}^{-1}$), dipping from a depth of 40 km in the west of the study area to a depth of about 100 km, at which level it remains to the eastern limit of the CF array. This slab is overlain by a mantle wedge of intermediate velocities ($V_p = 7.3\text{--}7.8 \text{ km s}^{-1}$). The gravity and isostatic response of the obtained velocity models translated to densities, give a very good first-order fit of the observed Bouguer anomaly and topography, which provides significant support of the results from RF modelling.

The models reveal lower crustal bodies with high crustal velocities. These lower crustal bodies might represent intruded mafic lower crust, possibly alternating with serpentinised peridotite on top of a hydrated mantle wedge, terminated at depth by a slab of eclogitised mafic crust. The nature of the crustal intrusion is not known, but presuming that it experienced increased temperatures after its emplacement, we prefer a subduction related pre-rift origin.

Break-up related igneous products can be expected in more distal parts of the margin, further east of the study area and at a sufficient distance from the serpentinite, to preventing it from retrogressing (see above). For the flat subduction mode, indicated by the slab geometry, we might expect less intense but widespread igneous activity, which is also consistent with our model. Serpentinisation and hydration of the mantle decrease with depth, indicated by increasing mantle velocities.

The topography is very likely to be isostatically compensated within the lithosphere, as illustrated by the direct response of the velocity model, and therefore does not require any significant additional dynamic support from the sublithospheric mantle. It seems that the crust of up to 40 km thickness in the west of the profile is able to support the highest topography of 1000–1500 m, whereas in the east, the thinner crust is not sufficient, and the identified mantle

wedge accounts for the additional support of the topography. We can therefore conclude that dynamic topography at this location on the East Greenland margin must be very limited. Since thick crust to the west is likely to be of Caledonian origin (continent-continent collision), it follows that the associated high topography seems best explained as a remnant from the Palaeozoic Caledonian orogeny, and isostatically supported by structures within the lithosphere. The Neogene uplift hypothesis is therefore not supported by our observations.

In summary, our results robustly suggest the existence of a fossil Caledonian subduction zone. The topography seems to be isostatically supported by the lithosphere. Possible implications for the larger image of orogenic and topographic evolution and structural relations remain open for further discussion and testing.

ACKNOWLEDGEMENTS

The installation and maintenance of the Central Fjord Array in East Greenland, project expenses including this study were financed as part of the project ‘Topography of the North Atlantic Realm’ (TOPOREAL), funded by the Danish Council for Independent Research (DFR). We thank DFR, all involved participants of TOPOREAL and all others who contributed to discussion of the results. We are grateful to two anonymous reviewers for very helpful and constructive comments, and to J. Richard Wilson and Lone Davidson who improved the English text.

REFERENCES

- Ammon, C.J., 1991. The isolation of receiver effects from teleseismic *P* waveforms, *Bull. seism. Soc. Am.*, **81**, 2504–2510.
- Ammon, C.J., Randall, G.E. & Zandt, G., 1990. On the nonuniqueness of receiver function inversions, *J. geophys. Res.: Solid Earth*, **95**, 15 303–15 318.
- Andersen, O.B., Knudsen, P. & Berry, P.A.M., 2009. The DNSC08GRA global marine gravity field from double retracked satellite altimetry, *J. Geodyn.*, **84**, 191–199.
- Andersen, T.B., Jamtveit, B., Dewey, J.F. & Swenson, E., 1991. Subduction and exhumation of continental crust: major mechanisms during continent-continent collision and orogenic extensional collapse, a model based on the south Norwegian Caledonides, *Terra Nova*, **3**, 303–310.
- Anderson, D.L., 2007. *New Theory of the Earth*, Cambridge Univ. Press.
- Andréasson, P.G., Gee, D.G., Whitehouse, M.J. & Schöberg, H., 2003. Subduction-flip during Iapetus Ocean closure and Baltica-Laurentia collision, Scandinavian Caledonides, *Terra Nova*, **15**, 362–369.
- Audet, P., 2013. Seismic anisotropy of subducting oceanic uppermost mantle from fossil spreading, *Geophys. Res. Lett.*, **40**, 173–177.
- Augland, L.E., Andresen, A. & Corfu, F., 2010. Age, structural setting, and exhumation of the Liverpool Land eclogite terrane, East Greenland Caledonides, *Lithosphere*, **2**, 267–286.
- Balling, N., 1980. The land uplift in Fennoscandia, gravity field anomalies and isostasy, in *Earth Rheology, Isostasy and Eustasy*, pp. 297–321, ed. Möerner, N.-A., John Wiley and Sons.
- Balling, N., 2000. Deep seismic reflection evidence for ancient subduction and collision zones within the continental lithosphere of northwestern Europe, *Tectonophysics*, **329**, 269–300.
- Bostock, M.G., 1998. Mantle stratigraphy and evolution of the Slave province, *J. geophys. Res.*, **103**, 21 183–21 200.
- Bostock, M.G., 2013. The Moho in subduction zones, *Tectonophysics*, **609**, 547–557.
- Bostock, M.G., Hyndman, R.D., Rondenay, S. & Peacock, S.M., 2002. An inverted continental Moho and serpentinization of the forearc mantle, *Nature*, **417**, 536–538.
- Braun, A., Kim, H.R., Csatho, B. & von Frese, R.R.B., 2007. Gravity-inferred crustal thickness of Greenland, *Earth planet. Sci. Lett.*, **262**, 138–158.
- Brown, E.L. & Leshner, C.E., 2014. North Atlantic magmatism controlled by temperature, mantle composition and buoyancy, *Nat. Geosci.*, **7**, 820–824.
- Brueckner, H.K., 2006. Dunk, dunkless and re-dunk tectonics: a model for metamorphism, lack of metamorphism, and repeated metamorphism of HP/UHP terranes, *Int. Geol. Rev.*, **48**, 978–995.
- Brueckner, H.K. & van Roermund, H.L.M., 2004. Dunk tectonics: a multiple subduction/duction model for the evolution of the Scandinavian Caledonides, *Tectonics*, **23**, TC2004, doi:10.1029/2003TC001502.
- Cassidy, J.F., 1992. Numerical experiments in broadband receiver function analysis, *Bull. seism. Soc. Am.*, **82**, 1453–1474.
- Cassidy, J.F. & Ellis, R.M., 1993. *S* wave velocity structure of the Northern Cascadia Subduction Zone, *J. geophys. Res.: Solid Earth*, **98**, 4407–4421.
- Christensen, N.I., 1996. Poisson’s ratio and crustal seismology, *J. geophys. Res.: Solid Earth*, **101**, 3139–3156.
- Christensen, N.I. & Mooney, W.D., 1995. Seismic velocity structure and composition of the continental crust: a global view, *J. geophys. Res.: Solid Earth*, **100**, 9761–9788.
- Clayton, R.W. & Wiggins, R.A., 1976. Source shape estimation and deconvolution of teleseismic bodywaves, *Geophys. J. R. astr. Soc.*, **47**, 151–177.
- Clowes, R.M., White, D.J. & Hajnal, Z., 2010. Mantle heterogeneities and their significance: results from Lithoprobe seismic reflection and refraction—wide-angle reflection studies, *Can. J. Earth Sci.*, **47**, 409–443.
- Cocks, L.R.M. & Torsvik, T.H., 2005. Baltica from the late Precambrian to mid-Palaeozoic times: the gain and loss of a terrane’s identity, *Earth-Sci. Rev.*, **72**, 39–66.
- Cocks, L.R.M. & Torsvik, T.H., 2011. The Palaeozoic geography of Laurentia and western Laurussia: a stable craton with mobile margins, *Earth-Sci. Rev.*, **106**, 1–51.
- Corfu, F., Andersen, T.B. & Gasser, D., 2014. The Scandinavian Caledonides: main features, conceptual advances and critical questions, *Geol. Soc. Lond. Spec. Publ.*, **390**, 9–43.
- Dahl-Jensen, T. *et al.*, 2003. Depth to Moho in Greenland: receiver-function analysis suggests two Proterozoic blocks in Greenland, *Earth planet. Sci. Lett.*, **205**, 379–393.
- Darbyshire, F.A., 2003. Crustal structure across the Canadian High Arctic region from teleseismic receiver function analysis, *Geophys. J. Int.*, **152**, 372–391.
- Darbyshire, F.A. *et al.*, 2004. A first detailed look at the Greenland lithosphere and upper mantle, using Rayleigh wave tomography, *Geophys. J. Int.*, **158**, 267–286.
- Dewey, J.F., 2005. Orogeny can be very short, *Proc. Natl. Acad. Sci.*, **102**, 15 286–15 293.
- Dobrzhinetskaya, L.F., Eide, E.A., Larsen, R.B., Sturt, B.A., Trønnes, R.G., Smith, D.C., Taylor, W.R. & Posukhova, T.V., 1995. Microdiamond in high-grade metamorphic rocks of the Western Gneiss region, Norway, *Geology*, **23**, 597–600.
- Du, Z.J. & Foulger, G.R., 1999. The crustal structure beneath the north-west fjords, Iceland, from receiver functions and surface waves, *Geophys. J. Int.*, **139**, 419–432.
- Duesterhoeft, E., Quinteros, J., Oberhänsli, R., Bousquet, R. & de Capitani, C., 2014. Relative impact of mantle densification and eclogitization of slabs on subduction dynamics: a numerical thermodynamic/thermokinematic investigation of metamorphic density evolution, *Tectonophysics*, **637**, 20–29.
- Ebbing, J., 2007. Isostatic density modelling explains the missing root of the Scandes, *Nor. J. Geol.*, **87**, 13–20.
- Ebbing, J., England, R.W., Korja, T., Lauritsen, T., Olesen, O., Stratford, W. & Weidle, C., 2012. Structure of the Scandes lithosphere from surface to depth, *Tectonophysics*, **536–537**, 1–24.
- Eckhardt, C. & Rabbel, W., 2011. P-receiver functions of anisotropic continental crust: a hierarchic catalogue of crustal models and azimuthal waveform patterns, *Geophys. J. Int.*, **187**, 439–479.
- Egholm, D.L., Nielsen, S.B., Pedersen, V.K. & Lesemann, J.-E., 2009. Glacial effects limiting mountain height, *Nature*, **460**, 884–887.

- England, R.W. & Ebbing, J., 2012. Crustal structure of central Norway and Sweden from integrated modelling of teleseismic receiver functions and the gravity anomaly, *Geophys. J. Int.*, **191**, 1–11.
- Fechner, N. & Jokat, W., 1996. Seismic refraction investigations on the crustal structure of the western Jameson Land Basin, East Greenland, *J. geophys. Res.: Solid Earth*, **101**, 15 867–15 881.
- Fitton, J.G., Saunders, A.D., Norry, M.J., Hardarson, B.S. & Taylor, R.N., 1997. Thermal and chemical structure of the Iceland plume, *Earth planet. Sci. Lett.*, **153**, 197–208.
- Forsberg, R., 1986. Gravity measurements in Jameson Land and neighbouring parts of East Greenland: Meddelelser om Grønland, *Geoscience*, **15**, 1–23.
- Forsberg, R. & Kenyon, S., 2004. Gravity and geoid in the Arctic region—the Northern polar gap now filled: ESA-ESRIN, in *Proceedings of the Second International GOCE User Workshop*, GOCE, The Geoid and Oceanography.
- Fossen, H., 2010. Extensional tectonics in the North Atlantic Caledonides: a regional view, *Geol. Soc. Lond. Spec. Publ.*, **335**, 767–793.
- Foulger, G.R. & Anderson, D.L., 2005. A cool model for the Iceland hotspot, *J. Volc. Geotherm. Res.*, **141**, 1–22.
- Foulger, G.R., Natland, J.H. & Anderson, D.L., 2005. A source for Icelandic magmas in Remelted Iapetus crust, *J. Volc. Geotherm. Res.*, **141**, 23–44.
- Frassetto, A. & Thybo, H., 2013. Receiver function analysis of the crust and upper mantle in Fennoscandia—isostatic implications, *Earth planet. Sci. Lett.*, **381**, 234–246.
- Frederiksen, A.W. & Bostock, M.G., 2000. Modelling teleseismic waves in dipping anisotropic structures, *Geophys. J. Int.*, **141**, 401–412.
- Gaina, C., Werner, S.C., Saltus, R. & Maus, S., 2011. Chapter 3 Circum-Arctic mapping project: new magnetic and gravity anomaly maps of the Arctic, *Geol. Soc. Lond. Mem.*, **35**, 39–48.
- Gasser, D., 2013. The Caledonides of Greenland, Svalbard and other Arctic areas: status of research and open questions, *Geol. Soc. Lond. Spec. Publ.*, **390**, 93–129.
- Gee, D.G., 2005. Europe Scandinavian Caledonides (with Greenland), in *Encyclopedia of Geology*, pp. 64–74, eds Selley, R., Cocks, L.R.M. & Plimer, I.R., Elsevier.
- Gee, D.G., Fossen, H., Henriksen, N. & Higgins, A.K., 2008. From the early Paleozoic platforms of Baltica and Laurentia to the Caledonide orogen of Scandinavia and Greenland, *Episodes*, **31**(1), 44–51.
- Gernigon, L., Lucazeau, F., Brigaud, F., Ringenbach, J.-C., Planke, S. & Le Gall, B., 2006. A moderate melting model for the Vøring margin (Norway) based on structural observations and a thermo-kinematical modelling: implication for the meaning of the lower crustal bodies, *Tectonophysics*, **412**, 255–278.
- Gernigon, L., Ringenbach, J.-C., Planke, S. & Le Gall, B., 2004. Deep structures and breakup along volcanic rifted margins: insights from integrated studies along the outer Vøring Basin (Norway), *Mar. Petrol. Geol.*, **21**, 363–372.
- Gilotti, J.A. & McClelland, W.C., 2007. Characteristics of, and a tectonic model for, ultrahigh-pressure metamorphism in the overriding plate of the Caledonian Orogen, *Int. Geol. Rev.*, **49**, 777–797.
- Gilotti, J.A. & McClelland, W.C., 2011. Geochemical and geochronological evidence that the North-East Greenland ultrahigh-pressure terrane is Laurentian crust, *J. Geol.*, **119**, 439–456.
- Gilotti, J.A., McClelland, W.C. & Wooden, J.L., 2014. Zircon captures exhumation of an ultrahigh-pressure terrane, North-East Greenland Caledonides, *Gondwana Res.*, **25**, 235–256.
- Gradmann, S., Ebbing, J. & Fullea, J., 2013. Integrated geophysical modelling of a lateral transition zone in the lithospheric mantle under Norway and Sweden, *Geophys. J. Int.*, **194**, 1358–1373.
- Green, P.F., Lidmar-Bergström, K., Japsen, P., Bonow, J.M. & Chalmers, J.A., 2013. Stratigraphic landscape analysis, thermochronology and the episodic development of elevated, passive continental margins, *Geol. Surv. Den. Greenl. Bull.*, **30**, 1–150.
- Guillot, S., Schwartz, S., Reynard, B., Agard, P. & Prigent, C., 2015. Tectonic significance of serpentinites, *Tectonophysics*, **646**, 1–19.
- Gutscher, M.-A., Maury, R., Eissen, J.-P. & Bourdon, E., 2000a. Can slab melting be caused by flat subduction?, *Geology*, **28**, 535–538.
- Gutscher, M.-A., Spakman, W., Bijwaard, H. & Engdahl, E.R., 2000b. Geodynamics of flat subduction: seismicity and tomographic constraints from the Andean margin, *Tectonics*, **19**, 814–833.
- Hacker, B.R. & Gans, P.B., 2005. Continental collisions and the creation of ultrahigh-pressure terranes: petrology and thermochronology of nappes in the central Scandinavian Caledonides, *Bull. geol. Soc. Am.*, **117**, 117–134.
- Hattori, K.H. & Guillot, S., 2003. Volcanic fronts form as a consequence of serpentinite dehydration in the forearc mantle wedge, *Geology*, **31**, 525–528.
- Henriksen, N., 1999. Conclusion of the 1:500 000 mapping project in the Caledonian fold belt in North-East Greenland, *Geol. Greenl. Surv. Bull.*, **183**, 10–22.
- Henriksen, N. & Higgins, A.K., 2008. Geological research and mapping in the Caledonian orogen of East Greenland, 70°N–82°N, *Geol. Soc. Am. Mem.*, **202**, 1–27.
- Higgins, A.K. & Leslie, A.G., 2008. Architecture and evolution of the East Greenland Caledonides, in *The Greenland Caledonides*, GSA Memoirs 202, The Geological Society of America.
- Hilaret, N., Reynard, B., Wang, Y., Daniel, I., Merkel, S., Nishiyama, N. & Petitgirard, S., 2007. High-pressure creep of serpentine, interseismic deformation, and initiation of subduction, *Science*, **318**, 1910–1913.
- Holbrook, W.S. *et al.*, 2001. Mantle thermal structure and active upwelling during continental breakup in the North Atlantic, *Earth planet. Sci. Lett.*, **190**, 251–266.
- Hopper, J.R., Dahl-Jesnen, T., Holbrook, W.S., Larsen, H.C., Lizarralde, D., Korenaga, J., Kent, G.M. & Kelemen, P.B., 2003. Structure of the SE Greenland margin from seismic reflection and refraction data: implications for nascent spreading center subsidence and asymmetric crustal accretion during North Atlantic opening, *J. geophys. Res. B: Solid Earth*, **108**, EPM 13-1–13-22.
- Hyndman, R.D. & Peacock, S.M., 2003. Serpentinization of the forearc mantle, *Earth planet. Sci. Lett.*, **212**, 417–432.
- Iwamori, H., 1998. Transportation of H₂O and melting in subduction zones, *Earth planet. Sci. Lett.*, **160**, 65–80.
- Iwasaki, T., Sellevoll, M.A., Kanazawa, T., Veggeland, T. & Shimamura, H., 1994. Seismic refraction crustal study along the Sognefjord, south-west Norway, employing ocean-bottom seismometers, *Geophys. J. Int.*, **119**, 791–808.
- Jacobsen, B.H. & Svenningsen, L., 2008. Enhanced uniqueness and linearity of receiver function inversion, *Bull. seism. Soc. Am.*, **98**, 1756–1767.
- Japsen, P. & Chalmers, J.A., 2000. Neogene uplift and tectonics around the North Atlantic: overview, *Glob. planet. Change*, **24**, 165–173.
- Ji, S., Li, A., Wang, Q., Long, C., Wang, H., Marcotte, D. & Salisbury, M., 2013. Seismic velocities, anisotropy, and shear-wave splitting of antigorite serpentinites and tectonic implications for subduction zones, *J. geophys. Res.: Solid Earth*, **118**, 1015–1037.
- Johnston, S.M., Hartz, E.H., Brueckner, H.K. & Gehrels, G.E., 2010. U–Pb zircon geochronology and tectonostratigraphy of southern Liverpool Land, East Greenland: implications for deformation in the overriding plates of continental collisions, *Earth planet. Sci. Lett.*, **297**, 512–524.
- Julià, J., Ammon, C.J., Herrmann, R.B. & Correig, A.M., 2000. Joint inversion of receiver function and surface wave dispersion observations, *Geophys. J. Int.*, **143**, 99–112.
- Kalsbeek, F., Higgins, A.K., Jepsen, H.F., Frei, R. & Nutman, A.P., 2008. Granites and granites in the East Greenland Caledonides, *Geol. Soc. Am. Mem.*, **202**, 227–249.
- Karabinos, P., Samson, S.D., Hepburn, J.C. & Stoll, H.M., 1998. Taconian orogeny in the New England Appalachians: collision between Laurentia and the Shelburne Falls arc, *Geology*, **26**, 215–218.
- Kennett, B.L.N., 1983. *Seismic Wave Propagation in Stratified Media*, Cambridge Univ. Press.
- Kenyon, S., Forsberg, R. & Coakley, B., 2008. New gravity field for the Arctic, *EOS, Trans. Am. Geophys. Un.*, **89**, 289–290.
- Kinck, J.J., Husebye, E.S. & Larsson, F.R., 1993. The Moho depth distribution in Fennoscandia and the regional tectonic evolution from Archean to Permian times, *Precambrian Res.*, **64**, 23–51.

- Kind, R., Kosarev, G.L. & Petersen, N.V., 1995. Receiver functions at the stations of the German Regional Seismic Network (GRSN), *Geophys. J. Int.*, **121**, 191–202.
- Kind, R. *et al.*, 2002. Seismic images of crust and upper mantle beneath Tibet: evidence for Eurasian plate subduction, *Science*, **298**, 1219–1221.
- Köhler, A., Weidle, C. & Maupin, V., 2011. Directionality analysis and Rayleigh wave tomography of ambient seismic noise in southern Norway, *Geophys. J. Int.*, **184**, 287–300.
- Kolstrup, M.L. & Maupin, V., 2013. A Proterozoic boundary in southern Norway revealed by joint-inversion of P-receiver functions and surface waves, *Precambrian Res.*, **238**, 186–198.
- Kolstrup, M.L., Pascal, C. & Maupin, V., 2012. What compensates the topography of southern Norway? Insights from thermo-isostatic modeling, *J. Geodyn.*, **61**, 105–119.
- Korenaga, J., 2004. Mantle mixing and continental breakup magmatism, *Earth planet. Sci. Lett.*, **218**, 463–473.
- Korenaga, J. & Kelemen, P.B., 2000. Major element heterogeneity in the mantle source of the North Atlantic igneous province, *Earth planet. Sci. Lett.*, **184**, 251–268.
- Korenaga, J., Holbrook, W.S., Kent, G.M., Kelemen, P.B., Detrick, R.S., Larsen, H.-C., Hopper, J.R. & Dahl-Jensen, T., 2000. Crustal structure of the southeast Greenland margin from joint refraction and reflection seismic tomography, *J. geophys. Res.: Solid Earth*, **105**, 21 591–21 614.
- Kosarev, G., Kind, R., Sobolev, S.V., Yuan, X., Hanka, W. & Oreshin, S., 1999. Seismic evidence for a detached Indian lithospheric mantle beneath Tibet, *Science*, **283**, 1306–1309.
- Kumar, P., Kind, R., Priestley, K. & Dahl-Jensen, T., 2007. Crustal structure of Iceland and Greenland from receiver function studies, *J. geophys. Res.: Solid Earth*, **112**, doi:10.1029/2005JB003991.
- Kvarven, T., Ebbing, J., Mjelde, R., Faleide, J.I., Libak, A., Thybo, H., Flueh, E.R. & Murai, Y., 2014. Crustal structure across the Møre margin, mid-Norway, from wide-angle seismic and gravity data, *Tectonophysics*, **626**, 21–40.
- Langston, C.A., 1979. Structure under Mount Rainier, Washington, inferred from teleseismic body waves, *J. geophys. Res.: Solid Earth*, **84**, 4749–4762.
- Larsen, H.C. & Saunders, A.D., 1998. Tectonism and volcanism at the Southeast Greenland Rifted Margin: a record of plume impact and later continental rapture, in *Proceedings of the Ocean Drilling Program, Scientific Results*.
- Leslie, A.G., Smith, M. & Scoper, N.J., 2008. Laurentian margin evolution and the Caledonian orogeny—a template for Scotland and East Greenland, in *The Greenland Caledonides*, GSA Memoirs 202, The Geological Society of America.
- Lidmar-Bergström, K. & Näsland, J.O., 2002. Landforms and uplift in Scandinavia, *Geol. Soc. Lond. Spec. Publ.*, **196**, 103–116.
- Manatschal, G., Froitzheim, N., Rubenach, M. & Turrin, B.D., 2001. The role of detachment faulting in the formation of an ocean-continent transition: insights from the Iberia Abyssal Plain, *Geol. Soc. Lond. Spec. Publ.*, **187**, 405–428.
- Mandler, H.A.F. & Jokat, W., 1998. The crustal structure of Central East Greenland: results from combined land–sea seismic refraction experiments, *Geophys. J. Int.*, **135**, 63–76.
- Maupin, V. *et al.*, 2013. The deep structure of the Scandes and its relation to tectonic history and present-day topography, *Tectonophysics*, **602**, 15–37.
- Medvedev, S. & Hartz, E.H., 2015. Evolution of topography of post-Devonian Scandinavia: effects and rates of erosion, *Geomorphology*, **231**, 229–245.
- Medvedev, S., Souche, A. & Hartz, E.H., 2013. Influence of ice sheet and glacial erosion on passive margins of Greenland, *Geomorphology*, **193**, 36–46.
- Menke, W., 1989. *Geophysical Data Analysis: Discrete Inverse Theory*, Academic Press.
- Menzies, M.A., Klemperer, S.L., Ebinger, C.J. & Baker, J., 2002. Characteristics of volcanic rifted margins, *Geol. Soc. Am. Spec. Pap.*, **362**, 1–14.
- Mercier, J.-P., Bostock, M.G., Audet, P., Gaherty, J.B., Garnero, E.J. & Revenaugh, J., 2008. The teleseismic signature of fossil subduction: Northwestern Canada, *J. geophys. Res.: Solid Earth*, **113**, doi:10.1029/2007JB005127.
- Mjelde, R., Kasahara, J., Shimamura, H., Kamimura, A., Kanazawa, T., Kodaira, S., Raum, T. & Shiobara, H., 2002. Lower crustal seismic velocity-anomalies; magmatic underplating or serpentinized peridotite? Evidence from the Vøring Margin, NE Atlantic, *Mar. geophys. Res.*, **23**, 169–183.
- Mjelde, R., Goncharov, A. & Müller, R.D., 2013. The Moho: boundary above upper mantle peridotites or lower crustal eclogites? A global review and new interpretations for passive margins, *Tectonophysics*, **609**, 636–650.
- Nielsen, S.B., Gallagher, K., Egholm, D.L., Clausen, O.R. & Summerfield, M., 2009a. Reply to comment regarding the ICE-hypothesis, *J. Geodyn.*, **48**, 101–106.
- Nielsen, S.B. *et al.*, 2009b. The evolution of western Scandinavian topography: a review of Neogene uplift versus the ICE (isostasy–climate–erosion) hypothesis, *J. Geodyn.*, **47**, 72–95.
- Nikulin, A., Levin, V. & Park, J., 2009. Receiver function study of the Cascadia megathrust: evidence for localized serpentinization, *Geochem. Geophys. Geosyst.*, **10**, doi:10.1029/2009GC002376.
- Nirrengarten, M., Gernigon, L. & Manatschal, G., 2014. Lower crustal bodies in the Møre volcanic rifted margin: geophysical determination and geological implications, *Tectonophysics*, **636**, 143–157.
- Olafsson, I., Sundvor, E., Eldholm, O. & Grue, K., 1992. Møre margin: crustal structure from analysis of expanded spread profiles, *Mar. geophys. Res.*, **14**, 137–162.
- Osmundsen, P.T. & Ebbing, J., 2008. Styles of extension offshore mid-Norway and implications for mechanisms of crustal thinning at passive margins, *Tectonics*, **27**, TC6016, doi:10.1029/2007TC002242.
- Ottmøller, L. & Midzi, V., 2003. The crustal structure of Norway from inversion of teleseismic receiver functions, *J. Seismol.*, **7**, 35–48.
- Owens, T.J., Taylor, S.R. & Zandt, G., 1987. Crustal structure at Regional Seismic Test Network stations determined from inversion of broadband teleseismic P waveforms, *Bull. seism. Soc. Am.*, **77**, 631–662.
- Park, J., 2004. Subduction zone anisotropy beneath Corvallis, Oregon: a serpentinite skid mark of trench-parallel terrane migration?, *J. geophys. Res.*, **109**, doi:10.1029/2003JB002718.
- Peacock, S.M., 1993. Large-scale hydration of the lithosphere above subducting slabs, *Chem. Geol.*, **108**, 49–59.
- Pedersen, V.K., Egholm, D.L. & Nielsen, S.B., 2010. Alpine glacial topography and the rate of rock column uplift: a global perspective, *Geomorphology*, **122**, 129–139.
- Pérez-Gussinyé, M., Ranero, C.R., Reston, T.J. & Sawyer, D., 2003. Mechanisms of extension at nonvolcanic margins: evidence from the Galicia interior basin, west of Iberia, *J. geophys. Res. B: Solid Earth*, **108**, EPM 6–1–6–19.
- Queyfi, J. & Clowes, R.M., 2010. Paleoproterozoic subduction in northwestern Canada from near-vertical and wide-angle seismic reflection data, *Can. J. Earth Sci.*, **47**, 35–52.
- Reynard, B., 2013. Serpentine in active subduction zones, *Lithos*, **178**, 171–185.
- Rickers, F., Fichtner, A. & Trampert, J., 2013. The Iceland–Jan Mayen plume system and its impact on mantle dynamics in the North Atlantic region: evidence from full-waveform inversion, *Earth planet. Sci. Lett.*, **367**, 39–51.
- Roberts, D., 2003. The Scandinavian Caledonides: event chronology, palaeogeographic settings and likely modern analogues, *Tectonophysics*, **365**, 283–299.
- Rondenay, S., Abers, G.A. & van Keken, P.E., 2008. Seismic imaging of subduction zone metamorphism, *Geology*, **36**, 275–278.
- Sandvol, E., Seber, D., Barazangi, M., Vernon, F., Mellors, R. & Al-Amri, A., 1998a. Lithospheric seismic velocity discontinuities beneath the Arabian Shield, *Geophys. Res. Lett.*, **25**, 2873–2876.
- Sandvol, E., Seber, D., Calvert, A. & Barazangi, M., 1998b. Grid search modeling of receiver functions: implications for crustal structure in the Middle East and North Africa, *J. geophys. Res.: Solid Earth*, **103**, 26 899–26 917.

- Saunders, A.D., Fitton, J.G., Kerr, A.C., Norry, M.J. & Kent, R.W., 1997. The North Atlantic igneous province, in *Large Igneous Provinces: Continental, Oceanic, and Planetary Flood Volcanism*, pp. 45–93, eds Honey, J. & Coffin, M.F., American Geophysical Union.
- Schiffer, C., Balling, N., Jacobsen, B.H., Stephenson, R.A. & Nielsen, S.B., 2014. Seismological evidence for a fossil subduction zone in the East Greenland Caledonides, *Geology*, **42**, 311–314.
- Schindwein, V. & Jokat, W., 1999. Structure and evolution of the continental crust of northern east Greenland from integrated geophysical studies, *J. geophys. Res.*, **104**, 15 227–15 245.
- Schindwein, V. & Jokat, W., 2000. Post-collisional extension of the East Greenland Caledonides: a geophysical perspective, *Geophys. J. Int.*, **140**, 559–567.
- Schmidt, S., Götze, H.J., Fichler, C. & Alvers, M., 2010. IGMAS+—a new 3D gravity, FTG and magnetic modeling software, in *Konferenzband GEO-INFORMATIK 2010 Die Welt im Netz, Herausgeber*, pp. 57–63, Akademische Verlagsgesellschaft AKA GmbH.
- Schmidt-Aursch, M.C. & Jokat, W., 2005. The crustal structure of central East Greenland—II: from the Precambrian shield to the recent mid-oceanic ridges, *Geophys. J. Int.*, **160**, 753–760.
- Schulte-Pelkum, V. & Mahan, K.H., 2014. A method for mapping crustal deformation and anisotropy with receiver functions and first results from USArray, *Earth planet. Sci. Lett.*, **402**, 221–233.
- Shao, T. et al., 2014. Antigorite-induced seismic anisotropy and implications for deformation in subduction zones and the Tibetan Plateau: antigorite-induced seismic anisotropy, *J. geophys. Res.: Solid Earth*, **119**, 2068–2099.
- Skogseid, J., Planke, S., Faleide, J.I., Pedersen, T., Eldholm, O. & Neverdal, F., 2000. NE Atlantic continental rifting and volcanic margin formation, *Geol. Soc. Lond. Spec. Publ.*, **167**, 295–326.
- Song, T.-R.A. & Kim, Y., 2011. Anisotropic uppermost mantle in young subducted slab underplating Central Mexico, *Nat. Geosci.*, **5**, 55–59.
- Steltenpohl, M., Hames, W., Andresen, A. & Markl, G., 2003. New Caledonian eclogite province in Norway and potential Laurentian (Taconic) and Baltic links, *Geology*, **31**, 985–988.
- Stratford, W. & Thybo, H., 2011. Seismic structure and composition of the crust beneath the southern Scandes, Norway, *Tectonophysics*, **502**, 364–382.
- Svenningsen, L. & Jacobsen, B.H., 2007. Absolute S-velocity estimation from receiver functions, *Geophys. J. Int.*, **170**, 1089–1094.
- Svenningsen, L., Balling, N., Jacobsen, B.H., Kind, R., Wylegalla, K. & Schweitzer, J., 2007. Crustal root beneath the highlands of southern Norway resolved by teleseismic receiver functions, *Geophys. J. Int.*, **170**, 1129–1138.
- Tegner, C., Leshner, C.E., Larsen, L.M. & Watt, W.S., 1998. Evidence from the rare-earth-element record of mantle melting for cooling of the Tertiary Iceland plume, *Nature*, **395**, 591–594.
- Tarantola, A. & Valette, B., 1982. Generalized nonlinear inverse problems solved using the least squares criterion, *Rev. Geophys.*, **20**, 219–232.
- Turcotte, D.L. & Schubert, G., 2002. *Geodynamics*, Cambridge Univ. Press.
- Ulmer, P. & Trommsdorff, V., 1995. Serpentine stability to mantle depths and subduction-related magmatism, *Science*, **268**, 858–861.
- van der Velden, A.J. & Cook, F.A., 2005. Relict subduction zones in Canada, *J. geophys. Res.: Solid Earth*, **110**, doi:10.1029/2004JB003333.
- van Hunen, J., van den Berg, A.P. & Vlaar, N.J., 2002. On the role of subducting oceanic plateaus in the development of shallow flat subduction, *Tectonophysics*, **352**, 317–333.
- van Hunen, J., van den Berg, A.P. & Vlaar, N.J., 2004. Various mechanisms to induce present-day shallow flat subduction and implications for the younger Earth: a numerical parameter study, *Phys. Earth planet. Inter.*, **146**, 179–194.
- van Roermund, H.L.M. & Drury, M.R., 1998. Ultra-high pressure ($P > 6$ GPa) garnet peridotites in Western Norway: exhumation of mantle rocks from > 185 km depth, *Terra Nova*, **10**, 295–301.
- Van Staal, C.R., Dewey, J.F., Niocail, C.M. & McKerrow, W.S., 1998. The Cambrian-Silurian tectonic evolution of the northern Appalachians and British Caledonides: history of a complex, west and southwest Pacific-type segment of Iapetus, *Geol. Soc. Lond. Spec. Publ.*, **143**, 197–242.
- van Staal, C.R., Whalen, J.B., Valverde-Vaquero, P., Zagorevski, A. & Rogers, N., 2009. Pre-Carboniferous, episodic accretion-related, orogenesis along the Laurentian margin of the northern Appalachians, *Geol. Soc. Lond. Spec. Publ.*, **327**, 271–316.
- Vinnik, L.P., 1977. Detection of waves converted from P to SV in the mantle, *Phys. Earth planet. Inter.*, **15**, 39–45.
- Voss, M. & Jokat, W., 2007. Continent–ocean transition and voluminous magmatic underplating derived from P -wave velocity modelling of the East Greenland continental margin, *Geophys. J. Int.*, **170**, 580–604.
- Voss, M., Schmidt-Aursch, M.C. & Jokat, W., 2009. Variations in magmatic processes along the East Greenland volcanic margin, *Geophys. J. Int.*, **177**, 755–782.
- Weigel, W. et al., 1995. Investigations of the East Greenland continental margin between 70° and 72° N by deep seismic sounding and gravity studies, *Mar. geophys. Res.*, **17**, 167–199.
- White, R.S., 1992. Crustal structure and magmatism of North Atlantic continental margins, *J. Geol. Soc.*, **149**, 841–854.
- Wiechert, E. & Zoeppritz, K., 1907. Über erdbebenwellen, *Nachrichten Von Ges. Wiss. Zu Gött. Math.-Phys. Kl.*, **1907**, 415–549.
- Worthington, J.R., Hacker, B.R. & Zandt, G., 2013. Distinguishing eclogite from peridotite: EBSD-based calculations of seismic velocities, *Geophys. J. Int.*, **193**, 489–505.
- Yoshinobu, A.S., Barnes, C.G., Nordgulen, Ø., Prestvik, T., Fanning, M. & Pedersen, R.B., 2002. Ordovician magmatism, deformation, and exhumation in the Caledonides of central Norway: an orphan of the Taconic orogeny?, *Geology*, **30**, 883–886.
- Zhu, L. & Kanamori, H., 2000. Moho depth variation in southern California from teleseismic receiver functions, *J. geophys. Res.: Solid Earth*, **105**, 2969–2980.

APPENDIX

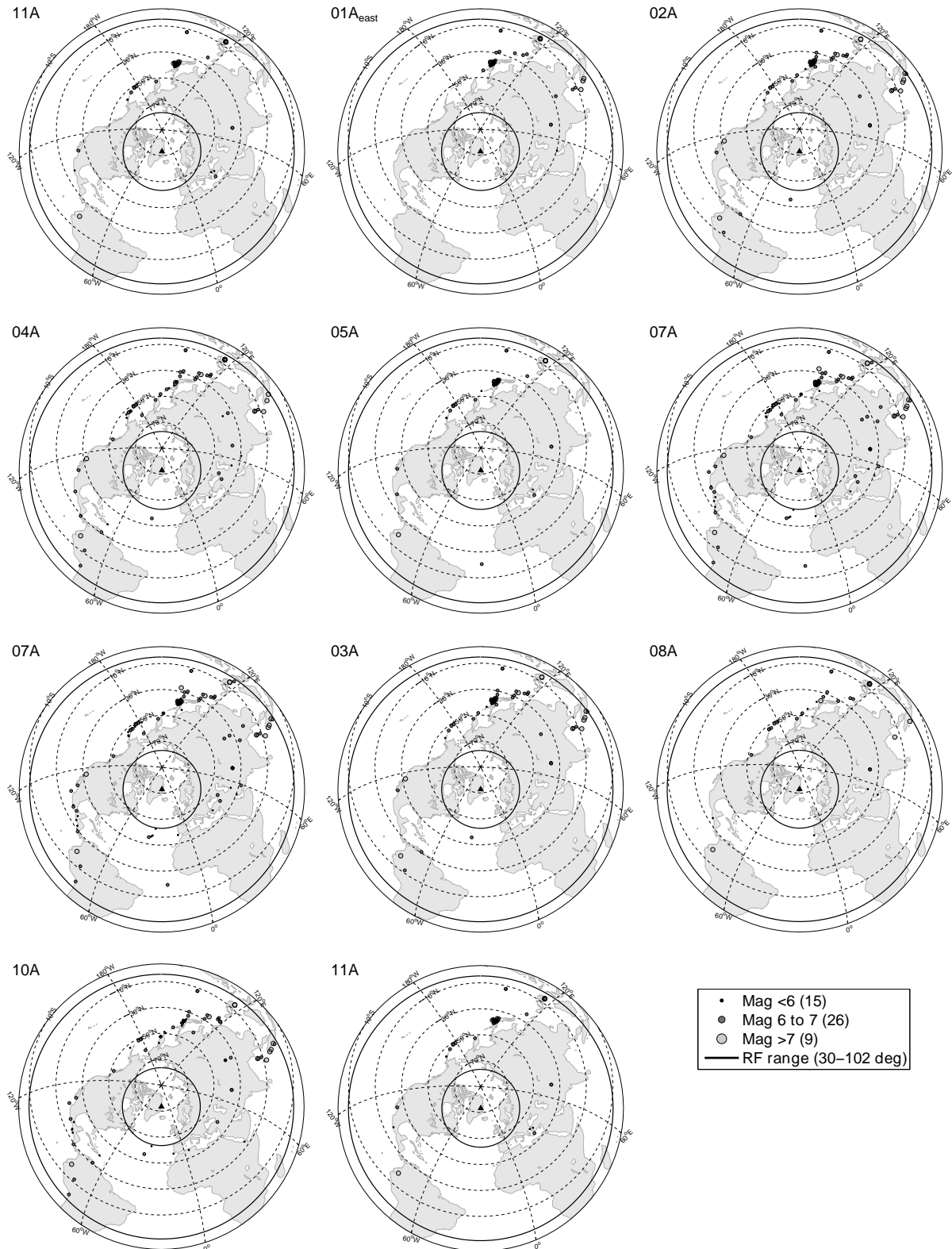


Figure A1. Used event locations for all stations (see Fig. 3 for details).

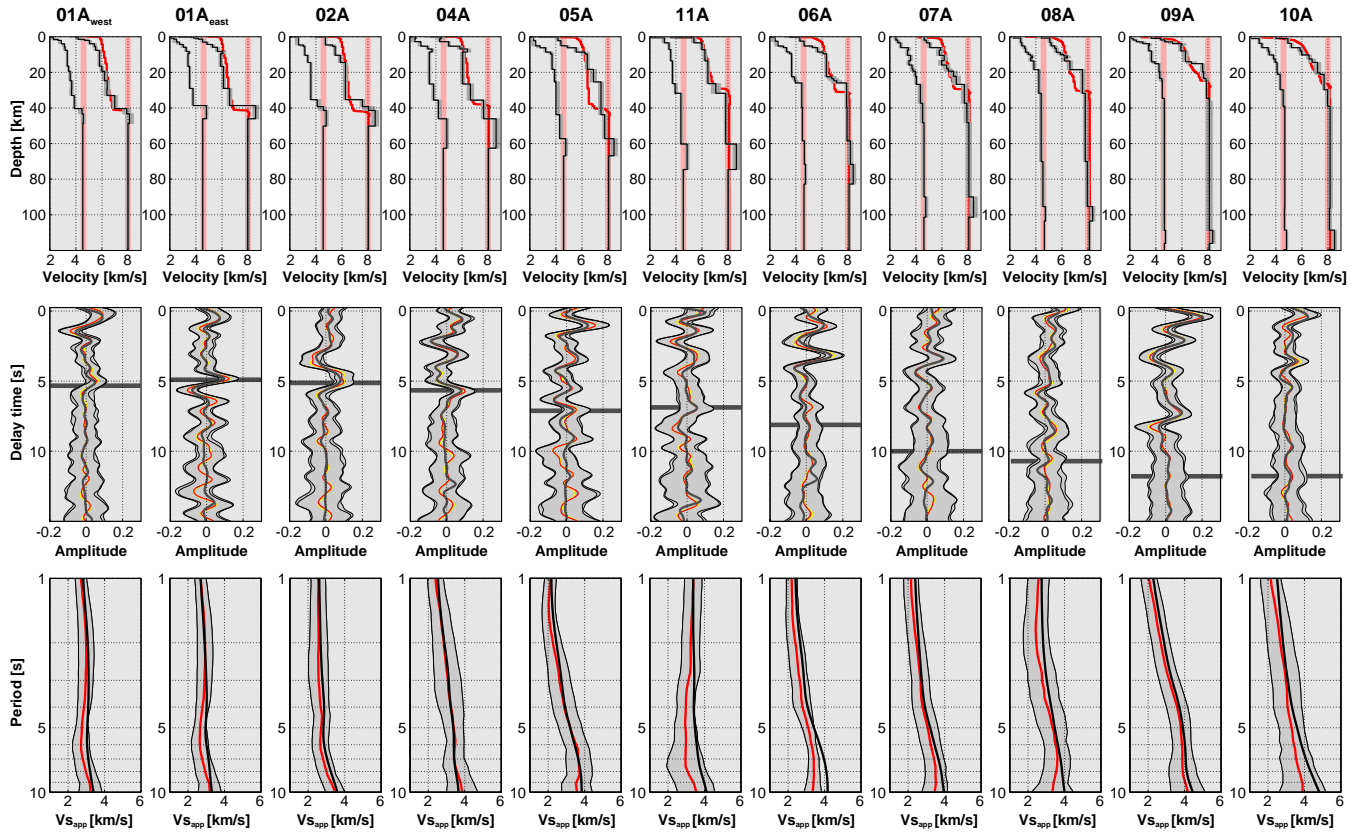


Figure A2. Receiver function inversion showing Q-RFs. Upper panel: final V_s and V_p velocities (black) and posterior standard deviation (grey shading, see text). Red is the prior model from wide-angle seismics. Red shading indicates standard mantle velocity of approximately $V_s = 4.6 \text{ km s}^{-1}$ and $V_p = 8.05 \text{ km s}^{-1}$. Middle panel: Q-receiver function waveforms. Black – synthetic RF. Yellow – small fraction stack. Red – large fraction stack. Grey shading – standard deviation of individual RFs. Dark grey horizontal line – delay time of the modelled upper slab interface. The waveforms of the two different stacking fractions are almost identical. Lower panel: $V_{s_{app}}$ curves. Red – observed (median of all events at one station). Black – synthetic $V_{s_{app}}$ curve.